

Effects of Cryogenic Temperature and Grain Size on Fatigue-Crack Propagation in the Medium-Entropy CrCoNi Alloy

Julian Rackwitz^{1,2+}, Qin Yu¹⁺, Yang Yang³, Guillaume Laplanche⁴, Easo. P. George^{5,6}, Andrew M. Minor^{3,7}, Robert O. Ritchie^{1,7}

¹Materials Sciences Division, Lawrence Berkeley National Laboratory, Berkeley, CA 94720, USA

²Department of Continuum Mechanics & Materials Theory, Tech. University of Berlin, 10623, Germany

³National Center for Electron Microscopy, Molecular Foundry, Lawrence Berkeley National Laboratory, Berkeley, CA 94720, USA

⁴Institute for Materials, Ruhr University Bochum, D-44801 Bochum, Germany

⁵Materials Science and Technology Division, Oak Ridge National Laboratory, Oak Ridge, TN 37831, USA

⁶Department of Materials Science & Engineering, University of Tennessee, Knoxville, TN 37996, USA

⁷Department of Materials Science & Engineering, University of California, Berkeley, CA 94720, USA

*Corresponding author: R. O. Ritchie (roritchie@lbl.gov)

+These authors contributed equally to this work.

Abstract: CrCoNi-based high-entropy alloys have demonstrated outstanding mechanical properties, particularly at cryogenic temperatures. Here we investigate the fatigue-crack propagation properties of the equiatomic, single-phase, face-centered cubic, medium-entropy alloy (MEA), CrCoNi, that displays exceptional strength, ductility and toughness, all of which are enhanced at cryogenic temperatures. Fatigue-crack growth is examined, at a load ratio of 0.1 over a wide range of growth rates, from $\sim 10^{-11}$ to $> 10^{-7}$ m/cycle, at room (293K) and cryogenic (198K, 77K) temperatures for two grain sizes (~7 and 68 μm), with emphasis on near-threshold behavior. We find that the ΔK_{th} fatigue thresholds are increased with decreasing temperature and increasing grain size: from 5.7 MPa $\sqrt{\text{m}}$ at 293K to 8 MPa $\sqrt{\text{m}}$ at 77K in the fine-grained alloy, and from 9.4 MPa $\sqrt{\text{m}}$ at 293K to 13.7 MPa $\sqrt{\text{m}}$ at 77K in the coarse-grained alloy. Mechanistically, transgranular cracking at 293K transitions to a mixture of intergranular and transgranular at cryogenic temperatures, where the increased propensity of nano-twins appears to inhibit growth rates by deflecting the crack path. However, the main factor affecting near-threshold behavior is roughness-induced crack closure from interference between the crack flanks, which is enhanced by the rougher fracture surfaces at low temperatures, particularly in the coarser-grained microstructure. Fatigue-crack propagation behavior in CrCoNi is comparable to nickel-based superalloys but is superior to that of the high-entropy CrMnFeCoNi (Cantor) alloy and many high-strength steels, making the CrCoNi alloy an excellent candidate material for safety-critical applications, particularly involving low temperatures.

Keywords: Medium-entropy alloy; fatigue-crack propagation; crack closure; cryogenic temperatures; grain size effects.

1. Introduction

With the ongoing demands of developing advanced structural materials, equiatomic multi-component metallic materials have recently gained enormous attention because of their promising mechanical properties including outstanding combinations of tensile strength, ductility and toughness as well as excellent corrosion and wear resistance [1–6]. First introduced almost two decades ago [7,8], alloys containing five or more elements in equiatomic concentrations, termed high-entropy alloys (HEAs)*, have recently been studied in earnest, in particular the face-centered cubic (*fcc*) CrCoNi-based alloys, which are often single-phase solid solutions, and the body-centered cubic (*bcc*) refractory multi-principal element alloys [9–11]. Whereas the latter alloys comprise combinations of several refractory elements in an attempt to realize high-temperature strength with room-temperature ductility [12,13], many of the CrCoNi-based alloys have shown exceptional mechanical properties at cryogenic temperatures [1,2,14,15]. For example, the earliest of these alloys, the so-called Cantor (CrMnFeCoNi) HEA, exhibits tensile strengths over 700 MPa, ductilities of ~70% and K_{Ic} fracture toughness values in excess of 200 MPa \sqrt{m} , properties that are further enhanced at cryogenic temperatures [1].

However, a derivative of the Cantor alloy, the *fcc*, single-phase, equiatomic CrCoNi medium-entropy alloy (MEA), has been found to display even better damage-tolerance with tensile strengths of ~1.3 GPa, ductilities of ~90% and K_{Ic} values of >270 MPa \sqrt{m} at liquid nitrogen temperatures [2]. This unusual simultaneous improvement in strength and ductility with decreasing temperature is attributed to an earlier onset of deformation twinning due to the higher strength at lower temperatures [16–18]. The generation of abundant nano-twin boundaries impedes dislocation motion and leads to an enhanced work-hardening ability, which delays the onset of the necking instability resulting in enhanced strength and ductility. Indeed, the CrCoNi alloy appears to possess the best combination of cryogenic-temperature strength and toughness on record, which furthers this alloy's potential for cutting-edge applications [2,14].

In contrast to the extensive studies on the mechanical properties of CrCoNi-based alloys [1,2,14,15], only limited research has been devoted to the fatigue properties of HEAs [19–40], despite the fact that fatigue will invariably be life-limiting for most potential structural

* This term was motivated by the notion that the high mixing entropies of five or more constituent elements could overcome the phase formation enthalpy to result in a single-phase solid-solution alloy [7], although it is now known that the high configuration entropy itself does not necessarily guarantee this [9].

applications. In fact, there is no published work to our knowledge on fatigue-crack growth in MEAs such as the CrCoNi alloy. Most early studies on the fatigue of HEAs were focused on clarifying the influence of processing variables on the stress/strain-life (*S-N*) behavior of CrCoNi-based alloy variants. Akin to many metallic materials, a linear correlation was found between the tensile strength and fatigue strength [22], with improvements to the fatigue resistance secured by processing procedures that minimized shrinkage pores and macro-segregation [26] or by reducing the grain size to ultra-fine scales [21,26,35,40]. Corresponding fatigue-crack propagation studies are much more limited, although cyclic crack-growth behavior in the Cantor CrMnFeCoNi alloy [28,33] has recently been shown to be similar to most comparable-strength structural alloys, but the all-important near-threshold fatigue resistance, and the specific values of the ΔK_{th} fatigue threshold, were both enhanced with decrease in temperature. Specifically, the fatigue threshold of the CrMnFeCoNi alloy (grain size $\sim 7 \mu\text{m}$) at a load ratio ($R = K_{\min}/K_{\max}$) of 0.1 increased from $\Delta K_{\text{th}} \sim 4.8 \text{ MPa}\sqrt{\text{m}}$ at room temperature to $\Delta K_{\text{th}} \sim 6.3 \text{ MPa}\sqrt{\text{m}}$ at 198K [28].

Considering the superior mechanical properties of CrCoNi compared to the CrMnFeCoNi alloy, it might be anticipated that the CrCoNi alloy would outperform the Cantor alloy in terms of its fatigue-crack growth resistance. Accordingly, the present study seeks to characterize the fatigue-crack propagation behavior of the CrCoNi MEA, with emphasis on the influence of temperature (293K, 198K *vs.* 77K) and grain size ($\sim 7 \mu\text{m}$ *vs.* $\sim 68 \mu\text{m}$), and to examine the microstructural origins of this behavior, in particular in terms of the mechanistic roles of crack closure and deformation nano-twinning.

2. Experimental procedures

2.1. Material

The CrCoNi alloy was vacuum-induction melted from equiatomic high-purity elemental constituents and cast into a cylindrical mold with a diameter of 45 mm. Subsequently, the cast ingot was thermally homogenized at 1473K for 48 h and rotary swaged at room temperature into a rod with a diameter of $\sim 17 \mu\text{m}$. These processing steps are similar to those employed in a previous study; further details are described in [16]. The swaged rod was finally recrystallized at 1073K for 1 h to achieve a single phase *fcc* alloy with a fine grain size of $\sim 7 \mu\text{m}$. To study the influence of the grain size on the fatigue-crack propagation behavior, the recrystallized fine-

grained rod was further annealed at 1173K for 1 h in an inert argon atmosphere, to produce an order of magnitude larger grain size of $\sim 68 \mu\text{m}$.

2.2. Mechanical characterization

The tensile properties of the fine- and coarse-grained CrCoNi alloys were measured using uniaxial tensile testing. Dog-bone shaped rectangular specimens with a gauge cross-section of $0.8 \times 1.5 \text{ mm}^2$ and a gauge length of 4.8 mm were machined from the fine- and coarse-grained rods with their flat surfaces aligned parallel to the rod's cross section. The loading direction of all the tensile specimens was aligned along the rod diameter. Uniaxial tensile tests were performed at three temperatures (293K, 198K, and 77K) on a 2 kN Instron 5594 universal testing system (Instron Corporation, Norwood, MA, USA) at an engineering strain rate of $8.0 \times 10^{-4} \text{ s}^{-1}$. Three tensile specimens were tested for each grain size at each temperature.

Fatigue-crack propagation behavior in the fine- and coarse-grained CrCoNi alloys was characterized using disc-shaped compact-tension DC(T) specimens. A total of 18 DC(T) specimens, with a width $W = 12.4 \text{ mm}$, thickness $B = 6.1 \text{ mm}$, and initial notch length $a_0 = 3.5 \text{ mm}$, were fabricated from the fine- and coarse-grained rods with their flat surfaces aligned parallel to the rod's cross section. The notch root radius of the DC(T) specimens was $\sim 100 \mu\text{m}$. Prior to testing, the specimen surfaces were ground using silicon carbide paper and polished to a $\sim 1\text{-}\mu\text{m}$ mirror finish using diamond suspension to allow for optical monitoring of the crack length.

To continuously monitor the length of the fatigue cracks, a uniaxial linear-patterned strain gauge (Vishay Precision Group, Raleigh, NC, USA) was attached to the centerline of the back-face of the specimen perpendicular to the notch direction. A model EA-06-031DE-350/LE strain gauge was used for testing in ambient air (293K) and dry ice (198K), while a model WK-13-031DE-350 strain gauge was used for testing in liquid nitrogen (77K). Crack lengths were derived from compliance measurements based on the back-face strain readings during the unloading portion of each cycle, using the relationship described by Gilbert *et al.* [41]:

$$\frac{a}{W} = 0.796239 + 5.40205 U - 103.821 U^2 + 714.676 U^3 - 2603.44 U^4 + 4829.01 U^5 - 3578.51 U^6, \quad (1)$$

$$\text{with } U = \frac{1}{\sqrt{-EBCW+1}}, \quad (2)$$

where E is Young's modulus, B is the specimen thickness, a and W are the crack length and the specimen width, respectively, and C is the compliance calculated as the reciprocal of the

unloading slope. The strain gauge was calibrated and checked for measurement accuracy during the pre-cracking stage, *i.e.* the crack lengths on both specimen surfaces were checked after unloading at interrupted steps using an optical microscope to ensure the calculated crack length reflected the actual crack length. In addition, the final crack length on the fracture surfaces of the tested specimens was used to verify the crack length calculated from the back-face strain. The validity of the calculated crack length was found to be within the range of $0.3 \leq a/W \leq 0.8$, beyond which measurement errors became significant probably due to strain gauge detachment at large deformation displacements; however, due to the limited linear range of the strain gauge, our tests were run only until $a/W \sim 0.7$.

Sinusoidal cyclic loading was performed using a 25 kN electro-servo hydraulic 810 MTS load frame (MTS Corporation, Eden Prairie, MN, USA) operated by an Instron 8800 digital controller (Instron Corporation, Norwood, MA, USA). All specimens were fatigue pre-cracked in ambient air at a frequency of 25 Hz by multiple steps of cyclic loading at constant amplitude to lower the stress-intensity range to a point where the plastic-zone size at the crack tip was below the anticipated plastic-zone size of the test starting point. The load ratio R , defined as the minimum load (or stress intensity) divided by the maximum load (or stress intensity) during a loading cycle, was set to 0.1. Between pre-cracking steps, the actual crack lengths on both sides of the specimen were checked using optical microscope to assure a symmetric crack growth, and an accurate measurement of the strain gauge.

The actual fatigue-crack propagation testing was conducted under constant-load and load-shedding conditions at a frequency of 25 Hz (sine wave) with a load ratio of $R = 0.1$, in accordance with the ASTM Standard E647 [42]. High crack-growth rates were characterized under constant-load conditions, in which the load amplitude was kept constant, such that the stress-intensity range ($\Delta K = K_{\max} - K_{\min}$) effectively increases as the crack advances. Near-threshold testing to characterize the threshold stress-intensity range (ΔK_{th}) was performed under load-shedding conditions, in which the applied external load was automatically decreased at a rate such that the imposed normalized K -gradient remained above -0.08 mm^{-1} , again in accordance with ASTM Standard E647 [42]. The fatigue threshold stress-intensity range, ΔK_{th} , was determined as the ΔK value at which the crack-propagation rate was reduced down to the range of $\sim 10^{-11}$ to $5 \times 10^{-10} \text{ m/cycle}$.

The influence of cryogenic temperature on fatigue-crack propagation in CrCoNi was examined at 293K, 198K and 77K. The room temperature testing was performed in ambient air,

whereas the cryogenic tests were conducted in immersion baths of dry ice in ethanol (198K) and liquid nitrogen (77K). To reach equilibrium at 198K and 77K, specimens were fully immersed in the cryogenic environment for at least 1 h prior to testing. The respective temperatures were maintained by frequently refilling dry-ice and liquid nitrogen without interruption throughout the test duration. All fatigue-crack growth data are presented as log-log plots of the crack-propagation rate, da/dN , as a function of stress-intensity range, ΔK , following a nominal Paris law formulation, *i.e.*, $da/dN \propto \Delta K^m$, where the Paris exponent, m , was measured in the mid-range of growth rates ($\sim 10^{-9}$ to $> 10^{-7}$ m/cycle).

2.3. Measurement of crack closure

A critical phenomenon that can occur during fatigue-crack growth is crack closure, which can be detected during the unloading of the fatigue loading cycle [43,44] from the physical contact of the mating crack surfaces before the minimum load/stress intensity is reached (Fig. 1). Specifically, while being unloaded, the specimen shows linear elastic behavior with a linear correlation between the load and the displacement, resulting in a constant compliance/stiffness value during the initial unloading stage. With further unloading, a change in the compliance/stiffness will be detected, which signifies the physical contact of the mating fracture surfaces. Accordingly, the occurrence of crack closure can be simply determined at the point of the slope change in the elastic compliance (or load-displacement) curve during the unloading cycle [45]. In practice, the closure point can be determined as the intersection of two linear fitted lines. One straight line is fitted to the load *vs.* back-face strain curve near the end of P_{\max} , whereas the other line is fitted to the load *vs.* back-face strain curve adjacent to the end of P_{\min} (Fig. 1). The load at the intersection of the two fitted lines is thus designated to the closure load P_{cl} . This compliance technique is regarded as an approximate but fairly practical one as compared to other quantitative estimates. Based on the determined closure load, P_{cl} , and the current crack length a , a closure stress intensity factor, K_{cl} , can be derived following:

$$K_{cl} = \frac{P_{cl}}{B\sqrt{W}} f\left(\frac{a}{W}\right), \quad (3)$$

where

$$f\left(\frac{a}{W}\right) = \frac{2+\frac{a}{W}}{\left(1-\frac{a}{W}\right)^{3/2}} \left[0.76 + 4.8\left(\frac{a}{W}\right) - 11.58\left(\frac{a}{W}\right)^2 + 11.43\left(\frac{a}{W}\right)^3 - 4.08\left(\frac{a}{W}\right)^4 \right], \quad (4)$$

in which the specific value of the a/W ratio was derived from the dimensionless compliance following from Eqs. (1) and (2). Based on the measurement of K_{cl} , the effective stress intensity range can be defined as $\Delta K_{eff} = K_{max} - K_{cl}$ when $K_{cl} > K_{min}$; $\Delta K_{eff} = \Delta K$ when $K_{cl} < K_{min}$.

2.4. Fractographic characterization

After fatigue testing, fractographic analysis was performed, using scanning electron microscopy, in an FEI Strata DB235 SEM (FEI Company, Portland, OR, USA) operated in the secondary electron (SE) imaging mode at 5-15 kV, to identify the salient deformation and fracture mechanisms involved in the crack propagation processes in both the coarse- and fine-grained structures at the three temperatures.

To specifically examine the corresponding crack-path profiles and discern the deformation mechanisms in the vicinity of the crack tip and crack wake under plane-strain conditions, some fatigued, but unbroken, DC(T) specimens were sliced through the thickness at the mid-thickness section. The interior surface (one half) was progressively polished to a 0.05 μm surface finish followed by a final vibration polishing using 0.05 μm colloidal silica for 12 h. The microstructure along the crack wake and the crack-tip region was characterized using electron back-scattered diffraction (EBSD) in an FEI Strata DB235 SEM (FEI Company, Portland, OR, USA) operated at 20 kV using a TEAM™ EBSD analysis system (Ametek EDAX, Mahwah, NJ, USA) at 35 nm, to specifically detect the occurrence of deformation twins.

To confirm the existence or absence of nano-twinning during the fatigue-crack propagation in the CrCoNi alloy, transmission electron microscopy (TEM) characterization was carried out on thin foils prepared by Ga⁺ focused ion beam (FIB) lift-out with a FEI Helios G4 machine. Thin films were taken from the plastic wake within a 12 μm depth beneath the fatigue fracture surface, parallel to the macroscopically-flat fatigue fracture surface. The beam energy used for thinning the sample was gradually reduced from 30 to 2 keV. TEM imaging of the nano-twins and dislocations was performed using an FEI (now ThermoFisher) TitanX or ThemIS TEM operated at 300 kV at the National Center for Electron Microscopy at the Lawrence Berkeley National Laboratory.

3. Results and discussion

3.1. Microstructure and tensile properties

The microstructures of the CrCoNi alloys were characterized using EBSD scans on the cross-section plane of the swaged and recrystallized (1073K for 1 h) rod as well as the subsequently annealed rod. As shown in the inverse pole figure (IPF) map (Fig. 2a), a uniform equiaxed grain structure with an average size of ~ 7 μm was developed in the swaged and recrystallized CrCoNi alloy. Further annealing led to an order of magnitude increase in average grain size to ~ 68 μm (Fig. 2b). In both fine and coarse grain structures, recrystallization (or annealing) twins could be observed, although their presence was far more evident in the coarse-grained microstructure.

Engineering stress-strain curves measured using dog-bone tensile specimens of the ~ 7 μm and ~ 68 μm grained-sized CrCoNi alloy are shown, respectively, in Figures 2c, d for temperatures of 293K, 198K and 77K. Corresponding values of the strength and ductility properties are listed in Table 1. Results show that the yield strength (σ_y) and tensile strength (σ_{uts}) of the fine-grained alloy at room temperature increase by 39% and 45%, respectively, to 728 MPa and 1290 MPa when the temperature was decreased to 77K. Similar trends are shown for the uniform elongation (ε_{ue}) and strain to failure (ε_f) properties which increase by 53% and 34%, respectively, to 0.51 and 0.58 at 77K. For the coarse-grained alloy, the yield and tensile strengths at room temperature increased by 68% and 44%, respectively, to 486 MPa and 1120 MPa when the temperature was decreased to 77K. Similarly, the uniform elongation and strain to failure increased by 22% and 12%, respectively, to 0.72 and 0.79 at 77K. A comparison between the tensile properties of the two microstructures at a given temperature clearly show that there is a trade-off between strength and ductility in the coarse- *vs.* fine-grained structures.

3.2. Fatigue-crack propagation behavior

Fatigue-crack propagation behavior in CrCoNi, at grain sizes of 7 μm and 68 μm , was examined at temperatures of 293K, 198K and 77K; results are displayed in Figure 3 in terms of the fatigue-crack growth rates, da/dN , from 10^{-11} to $>10^{-7}$ m/cycle, plotted as a function of the applied stress-intensity range ΔK . Similar to the strength and ductility properties (Table 1), the fatigue-crack growth resistance was found to improve with the decrease of temperature. Specifically, the threshold stress-intensity range (ΔK_{th}) for the fine-grained alloy increases by 40% from $\Delta K_{th} \sim 5.7$ $\text{MPa}\sqrt{\text{m}}$ at room temperature to $\Delta K_{th} \sim 8$ $\text{MPa}\sqrt{\text{m}}$ at 77K (Table 2, Fig. 3). Indeed, between 293K and 77K, a linear correlation can be established between the threshold stress-intensity range and the yield strength in the CrCoNi MEA (Fig. 4). Interestingly, the same

linear relationship applies to the CrMnFeCoNi HEA with a grain size same as the fine-grained CrCoNi MEA [28] ([Fig. 4](#)).

The trend of increasing thresholds at lower temperatures is further confirmed in the coarser-grained CrCoNi, which displays higher thresholds overall than the fine-grained material ([Figs. 3, 4](#)). At room temperature, the ΔK_{th} threshold for 68 μm grain size is 9.4 MPa $\sqrt{\text{m}}$, some 65% higher than that in the fine-grained structure; at 198K, the coarser-grained structure displays ΔK_{th} threshold of 11 MPa $\sqrt{\text{m}}$ *i.e.*, ~57% higher than in the fine-grained structure, and at 77K the ΔK_{th} threshold is further increased to 13.7 MPa $\sqrt{\text{m}}$, ~71% higher than in the fine-grained alloy ([Table 2, Fig. 3](#)). This trend of increasing fatigue thresholds with an increase in grain size is consistent with the experimental results on many materials, as shown, for example, by low strength steels [46] and α -titanium [47]. We believe that this effect in the CrCoNi MEA can be attributed to more significant crack-tip shielding due to roughness-induced crack closure (an extrinsic crack wedging effect) resulting from the rougher crack surfaces in the larger-grained material; this is consistent with the fact that the effect of grain size is far more marked at near-threshold levels where the crack opening displacements (CODs) are smaller. Additionally, the higher strengths associated with the lower temperatures will also act to limit the CODs. The linear relationship between the ΔK_{th} threshold and the yield strength, for a given grain size ([Fig. 4](#)), is somewhat harder to explain but is not inconsistent with the smaller CODs leading to higher relative closure levels. However, this effect is likely associated with the reduced cyclic plasticity in the higher strength structures, which limits the intrinsic mechanism of crack advance. We will examine all these mechanisms further in section 3.4 below where we discuss the issue of crack closure.

At higher, intermediate growth rates above $\sim 10^{-9}$ m/cycle, where the influence of microstructure on fatigue-crack propagation is generally far less pronounced, the growth rates are still lower, at a given ΔK , in the coarse-grained material and in either material at lower temperatures, but the effect is far smaller than at near-threshold stress intensities. As discussed in the following section, we believe that this is associated with a much smaller influence of crack closure, shown by our measurements in [Figure 5](#), which can be related to the larger CODs at the higher ΔK s in this regime. The Paris exponents in this mid-range of growth rates were found to be roughly 3 for the fine-grained alloy at both ambient and cryogenic temperatures and for the coarse-grained alloy at 77K, whereas the coarse-grained alloy showed somewhat higher Paris exponents of ~3.9 at 293K and 198K ([Table 2](#)).

To evaluate the ASTM validity of the results in Figure 3, the ligament size requirement was checked for the measured ΔK s according to ASTM standard E647 [42]. The standard specifies the following requirement for the uncracked ligament size in high strain-hardening materials:

$$W - a \geq \frac{4}{\pi} \left(\frac{K_{\max}}{\sigma_{FS}} \right)^2, \quad (5)$$

where W and a are the C(T) specimen width and crack length, respectively. K_{\max} is the maximum stress-intensity factor in a loading cycle. σ_{FS} is the flow stress which is defined as the average of yield (σ_y) and tensile (σ_{uts}) strengths. Based on Eq. (5), the ASTM specimen size requirement was satisfied for our test specimens of the fine-grained CrCoNi alloy when the ΔK s were smaller than 35, 41, 43 MPa \sqrt{m} at 293K, 198K, 77K, respectively. This indicates that the fatigue-crack growth behavior for the fine-grained alloy fully conformed to ASTM standards for growth rates up to approximately 10⁻⁷ m/cycle. For the coarse-grained alloy, this requirement was satisfied for the entire range of the growth rates. Accordingly, we can conclude that our measured fatigue-crack growth rates can be deemed to be independent of specimen size, except at the highest growth rates in the finer-grained alloy.

3.3. Crack closure results

As noted above, one of the major phenomena that can occur during fatigue-crack propagation is crack closure from physical contact of the mating crack surfaces. While there are different underlying mechanisms that can account for crack closure, the most ubiquitous source is roughness-induced crack closure, which originates from the local contact between fracture surface asperities, caused by small variations in the mode II displacements of the neighboring crack flanks, as the mating crack surface come into contact [48,49]. As it is a wedging process, it becomes most pronounced as the crack opening displacements become comparable with the size of these asperities [50], *i.e.*, at low, near-threshold stress intensities.

The variation of the degree of closure, in terms of the ratio of closure stress-intensity to the maximum stress intensity (K_{cl}/K_{\max}) as a function of the stress-intensity range (ΔK), is shown in Figure 5. In the mid-range of growth rates, here typically above a ΔK of ~15-20 MPa \sqrt{m} , the effect of crack closure becomes relatively small, and essentially independent of temperature and grain size, as the CODs, that scale with K^2 , become larger. However, with decreasing ΔK levels into the near-threshold regime, the degree of crack closure in both fine and coarse grain structures becomes progressively larger at all temperatures, primarily due to the increasingly smaller CODs as the ΔK s approach the threshold ΔK_{th} level. This increased crack-tip shielding in

the threshold region is further enhanced by the increased roughness of the fracture surfaces and the local shear displacements at the lower CODs in the near-threshold regime. As indicated from the measurements in [Figure 5](#), the coarse-grained material shows higher levels of crack closure which can be attributed to higher degree of roughness-induced crack closure originating from the rougher fracture surfaces in the coarser-grained material.

Using the estimated K_{cl} values measured over the entire range of the growth rates, we can approximately account for the effect of such closure on the mechanical driving force by estimating the effective stress-intensity range, ΔK_{eff} , as equal to $K_{max} - K_{cl}$ (when $K_{cl} > K_{min}$) and ΔK (when $K_{cl} \leq K_{min}$). Fatigue-crack propagation rates, da/dN , as a function of effective stress-intensity range ΔK_{eff} are plotted in [Figure 6a](#). To compare the results with and without consideration of the role of crack closure, we plot the da/dN vs. ΔK_{eff} curve and the da/dN vs. ΔK curve for the two grains sizes at each temperature ([Figs. 6b-c](#)). There is naturally little difference in these curves at the mid-range of growth rates where the effect of closure is relatively small; indeed, there is little effect of either temperature or grain size in this regime ([Fig. 6a](#)). At near-threshold levels, however, where there are significant differences in the growth-rate curves at the three temperatures and two grain sizes, taking account of crack closure, in terms of ΔK_{eff} , certainly does significantly diminish these differences, which indicates that it is a major factor in causing an effect of grain size and temperature on near-threshold behavior. Nevertheless, even with these measured K_{cl}/K_{max} values, the effects of grain size and temperature on the near-threshold crack-growth behavior cannot be fully accounted for, at least quantitatively, by our current estimation of crack closure ([Figs. 6b-c, Table 2](#)). Part of this may be associated with other factors that affect crack-growth rates – for example, crack deflection can also serve to promote crack-tip shielding – or simply due to the inherent difficulties of accurately measuring the precise values of the closure stress intensity.

3.4. Crack-path profiles and fractography

In order to understand the full effects of the temperature and grain size on the fatigue crack-growth resistance of the CrCoNi MEA, it is important to discern the fracture modes and the associated deformation mechanisms during crack propagation. As the fatigue resistance in the threshold regime is mostly affected by microstructure and temperature, we examined the crack-path profiles and the deformed microstructure in the plastic-wake regions at the mid-thickness (plane-strain) sections of fatigue tested samples by electron backscatter diffraction (EBSD) imaging. [Figure 7](#) presents the EBSD inverse pole figure (IPF) maps overlaid with the image

quality (IQ) maps showing the crack-path profiles for the fine- and coarse-grained alloys near the ΔK_{th} threshold at 293K, 198K and 77K. Specifically, [Figure 8](#) displays the tortuous crack paths that undergo significant crack deflection caused by interactions with deformation twins activated in the fine-and coarse-grained structures at 77K.

In parallel, we characterized the fracture morphology of the CrCoNi alloy in the near-threshold regime at all the investigated temperatures ([Fig. 9](#)). To confirm the existence or absence of nano-twinning in the threshold regime or at higher ΔK levels, TEM imaging of defects was also performed on thin foils prepared by FIB lift-out from the plastic wake within 12 μm depth beneath the fatigue fracture surface ([Fig. 10](#)).

At room temperature ([Fig. 7a](#)), the crack propagates predominantly in a transgranular mode, within the grains and through the recrystallization (or annealing) twins. The relatively lower image quality in certain regions neighboring the crack flanks indicates significant amount of plastic deformation, which is accommodated by the emission of dislocations at the crack tip subjected to the cyclic loading and unloading. In the CrCoNi alloy, the room temperature yield strength is relatively low, resulting in a larger amount of plastic deformation at a given ΔK value. Subsequently, the physical contact of the mating surfaces will leave a relatively large plastic wake, that could slightly flatten the crack path locally, thereby causing a loss of the contact shielding and leading to a marginal acceleration of the crack growth rate as compared to the lower temperatures where the yield strength is higher [51]. This mechanism, which was proposed to account for the reduced room-temperature fatigue threshold in CrMnFeCoNi [28], is believed to apply to the present CrCoNi as well. As confirmed from the EBSD orientation map ([Fig. 7a](#)) and the TEM micrograph ([Fig. 10a](#)), deformation twins were not detected in the plastic-wake regions in the fine-grained CrCoNi alloy at room temperature.

Correspondingly, the fracture morphology in the near-threshold regime at room temperature ([Fig. 9a](#)) reveals primarily transgranular crack propagation features. The transgranular fracture region is covered with periodic serrations having sharp edges orientated mainly perpendicular to the crack propagation direction ([Fig. 9a](#)), which are attributed to crack-tip blunting and resharpening due to cyclic plasticity [28]. Additionally, the sharp edges of serrations on some relatively large grains are flattened (see small white arrows in the inset of [Fig. 9a](#)), confirming that large plastic deformation has occurred locally, resulting in a loss of the contact shielding that is believed to lower the fatigue threshold at room temperature. The fractography of the coarse-grained structure in the near-threshold regime at 293K was similar to

that observed in the fine-grained alloy but naturally with coarser feature sizes due to the larger grain size ([Fig. 9b](#)).

Based on EBSD observations ([Fig. 7b](#)) and the TEM characterization ([Fig. 10b](#)), micro- and nano-scale deformation twins[†] were not identified after fatigue-crack propagation in the fine-grained alloy at 198K, akin to behavior at 293K. However, the fracture mode changed from predominantly transgranular at room temperature to a mixture of transgranular and intergranular fracture (white arrows in [Fig. 7b](#)). This is confirmed from the intergranular fracture morphology shown in a large fraction of the fracture surface (inset in [Fig. 9c](#)). The presence of intergranular fracture causes deviations in the crack path which serves to roughen the crack surface and thus enhance roughness-induced crack closure. The effect of such closure, induced by partial intergranular cracking at 198K, is reflected in the measured K_{cl}/K_{\max} values ([Fig. 5](#)) and the correspondingly higher fatigue thresholds compared to room temperature; specifically $\Delta K_{\text{th}} = 7 \text{ MPa}\sqrt{\text{m}}$ at 198K, which is 23% higher than the ΔK_{th} threshold of $5.7 \text{ MPa}\sqrt{\text{m}}$ at 293K. The fracture morphology of the coarse-grained alloy tested in the near-threshold regime at 198K ([Fig. 9d](#)) shares similar features as the fine-grained alloy showing a mixture of transgranular fracture and intergranular fracture, but with an increased fracture surface roughness due to the larger grain size, which promotes crack closure ([Fig. 5](#)) and thereby increases the fatigue threshold ([Fig. 3](#)).

However, when the temperature was further decreased to 77K, many deformation twins, with thicknesses of hundreds of nanometers (see TEM image in [Fig. 10c](#)) to a few micrometers, were observed in the fine-grained CrCoNi structure within ~1 to 3 grains of the crack path ([Figs. 7c, 8a](#)). As twinning is stress-controlled [52,53], this is likely motivated by the alloy's higher strength at lower temperatures which serves to activate deformation nano-twinning in the high stressed regions near the advancing crack tip. This results in a more transgranular fracture mode at 77K, with the crack path traversing through the grains, as well as along and across twin boundaries. As noted above, the crack path was frequently deflected by the dense nano-twins, either across the twin lamella or along the twin boundaries; this is shown in [Figures 7c](#) and [8a](#), and leads to numerous small-scale deviations of the crack path and even crack branching, which act to further promote roughness-induced closure. Correspondingly, the ΔK_{th} threshold at 77K is as high as $8 \text{ MPa}\sqrt{\text{m}}$, *i.e.*, respectively 14% and 40% higher than the thresholds at 198K and 293K.

[†] Some fine lamellar-shaped twins can be detected but are few in number; they are likely small recrystallization twins rather than deformation twins.

The fatigue fracture surface of the fine-grained alloy tested near the threshold at 77K ([Fig. 9e](#)) shows transgranular features with minor intergranular features. Similar to behavior at room temperature and at 198K, the transgranular fracture surface displays highly periodic serrations resulting from the cyclic plasticity. As deformation twinning is active at 77K due to the higher local stresses at the crack tip, such traces of twin lamella, with thicknesses in sub-micrometer scale, are visible on the fracture surface with alignments in different orientations (white arrows in the inset of [Fig. 9e](#)). Interestingly, the straight serrations generated by cyclic slip steps are deviated away from the crack propagation direction at the locations where profuse traces of nano-twins are evident. We believe this feature is indicative of the deviations in crack paths that originate from the deflection of the crack as it traverses the nano-twins ([Fig. 7c](#)).

In the coarse-grained CrCoNi alloy, crack propagation was largely transgranular at 293K with minor intergranular cracking ([Fig. 7d](#)). EBSD imaging shows evidence of crack deflection even at the annealing twins, either along the twin boundaries or across the twin lamella (white arrows in [Fig. 7d](#)); the annealing twins were developed during the heat treatment to coarsen the grain size (1 h at 1173K). The large grain size and the local crack-path deflections due to the profuse annealing twins both give rise to significantly coarser fracture surfaces and hence an increased effect of roughness-induced crack closure than in the fine-grained structure ([Fig. 5](#)). This contributed to the much higher ΔK_{th} threshold of 9.6 MPa \sqrt{m} in the coarse-grained structure, which is almost 70% higher than that for the fine-grained alloy. At 198K ([Fig. 7e](#)), similar to the fine-grained structure, the crack path was partly a mixture of transgranular cracking and intergranular cracking with some local crack deflection at the annealing twins, but as noted above, the coarser grains serve to develop a much rougher fracture surface, which promotes roughness-induced closure with a corresponding 63% higher ΔK_{th} threshold of 11.4 MPa \sqrt{m} at 198K than for the fine-grained structure.

At 77K, unlike the fine-grained structure, deformation twins were not detected in the coarse-grained alloy fatigued in the near-threshold regime. This is confirmed by EBSD imaging ([Fig. 7f](#)) and TEM examination ([Fig. 10d](#)). However, it is worth noting that, despite the absence of deformation twinning near the threshold $\Delta K_{th} \sim 13.7$ MPa \sqrt{m} at 77 K, fine traces of nano-twins with multiple variants surrounding the crack path can be seen at higher $\Delta K \sim 27.8$ MPa \sqrt{m} ([Fig. 8b](#)). The existence of nano-twins at higher ΔK in the coarse grains is further corroborated by the TEM characterization ([Fig. 10e](#)), where the formation of nano-scale twin-twin network is evident. Nevertheless, as inferred from the significant development of planar slip bands in the TEM image ([Fig. 10d](#)), crack propagation in the near-threshold regime in the coarse-grained

structure at 77K is predominantly driven by cyclic planar slip with local crack deflection at annealing twins (see white arrows in Fig. 7f). Due to the enlarged grain sizes, planar slip bands of multiple systems can be activated and intersected within the grain interior (Fig. 10d), which results in highly rough fracture morphology containing serrations with sharp edges oriented in more than one direction (inset in Fig. 9f). This rough transgranular morphology combined with the coarser-grained microstructure collectively enhances roughness-induced closure in the 68 μm structure (Fig. 5) such that the ΔK_{th} fatigue threshold at 77K rises to as high as 13.7 MPa $\sqrt{\text{m}}$, *i.e.*, over 70% higher than that measured for the fine-grained structure.

3.5. Comparison to other structural alloys

The fatigue-crack growth performance of the CrCoNi MEA is compared to that of the CrMnFeCoNi (Cantor) high-entropy alloy [1,28] as well as other comparable structural alloys - austenitic stainless steels [46], twinning-induced plasticity (TWIP) steels [54], and nickel-based superalloys [55–57] – in Figure 11; further details of these alloys and their mechanical properties are summarized in Table 3. The results listed were based on fatigue-crack growth experiments performed at room temperature at an R -ratio of 0.05 - 0.1.

As might be anticipated from the superior combination of tensile properties and fracture toughness of the CrCoNi alloy compared to the CrMnFeCoNi Cantor alloy [1,2], the fatigue crack-growth properties of the CrCoNi MEA outperforms the CrMnFeCoNi HEA as well [28]. The ΔK_{th} threshold fatigue thresholds of the fine-grained CrCoNi alloy at 293K and 198K are 19% and 11% higher, respectively, than those of the CrMnFeCoNi alloy with the same grain size. Similarly, it has superior fatigue threshold properties to the high-strength austenitic steels with low and moderate carbon contents [46], even though the grain size of the CrCoNi alloy is ~2 to 3 times smaller. It also has improved near-threshold properties at 293K when compared to several ultrahigh-strength low alloy steels that exhibit a ΔK_{th} threshold, *e.g.*, ~83% and 30% higher than that of 300-M steel and Fe-4Cr-0.35C steel, respectively. However, the fatigue-crack growth behavior of the fine-grained CrCoNi alloy is very similar to that of the TWIP steel with similar small grain size [54], with almost the same fatigue threshold at room temperature (Fig. 11).

With respect to the coarse-grained CrCoNi alloy, its fatigue crack-growth properties are comparable to nickel-based superalloys with similar large grain sizes [55–57]. Specifically, Inconel 718 with an intermediate grain size (22 μm) [56] has a threshold falling in between those of the fine- and coarse-grained CrCoNi, whereas large-grained (100 μm) Waspaloy is superior

to the coarse-grained CrCoNi with a 25% higher fatigue threshold, although it displays a 18% higher Paris exponent [55,57].

Overall, the CrCoNi MEA outperforms the Cantor alloy and common high-strength structural alloys in the terms of the excellent combination of tensile properties, fracture toughness, and fatigue-crack growth performance. Specifically, the enhanced strength, ductility, and fatigue threshold properties of the CrCoNi MEA, especially at low temperatures, render this alloy with a high potential as structural material for safety-critical engineering applications, especially at cryogenic temperatures.

4. Conclusions

Based on fatigue-crack propagation studies on the CrCoNi medium-entropy alloy, at a load ratio of $R = 0.1$ over a wide range of growth rates from $\sim 10^{-11}$ to $> 10^{-7}$ m/cycle, at room (293K) and cryogenic (198K and 77K) temperatures, for two grain sizes $\sim 7 \mu\text{m}$ and $68 \mu\text{m}$, the following conclusions can be drawn:

- Although the Paris exponents for the mid-range of growth rates are comparable ($m \sim 2.7 - 3.9$), reducing the test temperature from 293K to 77K results in a distinct increase in fatigue-crack growth resistance and in particular an increase in the ΔK_{th} fatigue threshold stress intensity.
- This effect is more pronounced in the coarse-grained alloy. Specifically, the ΔK_{th} thresholds for the fine-grain alloy were $5.7 \text{ MPa}\sqrt{\text{m}}$ at 298K, $7 \text{ MPa}\sqrt{\text{m}}$ at 198K, and $8 \text{ MPa}\sqrt{\text{m}}$ at 77K, whereas corresponding values for the coarse-grained alloy were roughly 60 to 70% higher at $9.4 \text{ MPa}\sqrt{\text{m}}$ at 293K and $11 \text{ MPa}\sqrt{\text{m}}$ at 198K and $13.7 \text{ MPa}\sqrt{\text{m}}$ at 77K.
- Mechanistically, roughness-induced crack closure appears to play a critical role in enhancing the fatigue thresholds at lower temperatures and in the coarse-grained microstructure. Compliance measurements of the closure loads during the fatigue-crack growth tests revealed higher levels of crack closure in the coarser-grained alloy.
- The enhanced roughness-induced crack closure at near-threshold levels results from the smaller crack-opening displacements at low ΔK levels and several factors which enhance the roughness of the fracture surfaces, especially in the coarse-grained microstructure. These factors include the incidence of a partial intergranular mode at 198K and the role of both annealing and deformation twins in deflecting the crack path. The latter mechanism is particularly active in fine-grained alloy at 77K where the high strength of the alloy and the

high tensile stresses in the crack-tip region promote profuse deformation twinning in the vicinity of the crack; such twins are not observed during fatigue-crack growth in the fine- and coarse-grained alloys at 293K and 198K.

- In terms of its fatigue-crack propagation resistance, the CrCoNi MEA outperforms the CrMnFeCoNi (Cantor) high-entropy alloy, especially at near-threshold stress intensities. The alloy exhibits crack-growth properties comparable to many high-strength conventional and advanced metallic structural alloys. Considering its excellent combination of strength, tensile ductility, fracture toughness and fatigue-crack growth resistance, all of which are enhanced with decrease in temperature, the CrCoNi MEA represents an outstanding structural alloy for safety-critical applications, particularly at cryogenic temperatures.

Acknowledgements

This work was supported by the U.S. Department of Energy, Office of Science, Office of Basic Energy Sciences, Materials Sciences and Engineering Division under contract no. DE-AC02-05-CH11231 to the Mechanical Behavior of Materials Program (KC13) at the Lawrence Berkeley National Laboratory (LBNL). E.P.G. was supported by the U.S. Department of Energy, Office of Science, Basic Energy Sciences, Materials Sciences and Engineering Division at the Oak Ridge National Laboratory. EBSD and TEM microscopy was carried out at LBNL's Molecular Foundry supported by the Office of Science, Office of Basic Energy Sciences, of the U.S. Department of Energy under contract no. DE-AC02-05-CH11231. G.L. acknowledges funding from the German Research Foundation (DFG) through project LA 3607/1-1. The authors gratefully acknowledge the preliminary work done by Dr. Keli V.S. Thurston in helping to set up some of the testing protocols.

References

- [1] B. Gludovatz, A. Hohenwarter, D. Catoor, E.H. Chang, E.P. George, R.O. Ritchie, A fracture-resistant high-entropy alloy for cryogenic applications, *Science* 345 (2014) 1153–1158. doi:10.1126/science.1254581.
- [2] B. Gludovatz, A. Hohenwarter, K.V.S. Thurston, H. Bei, Z. Wu, E.P. George, R.O. Ritchie, Exceptional damage-tolerance of a medium-entropy alloy CrCoNi at cryogenic temperatures, *Nat. Commun.* 7 (2016) 1–8. doi:10.1038/ncomms10602.
- [3] E.P. George, D. Raabe, R.O. Ritchie, High-entropy alloys, *Nat. Rev. Mater.* 4 (2019) 515–534.

doi:10.1038/s41578-019-0121-4.

- [4] E.P. George, W.A. Curtin, C.C. Tasan, High entropy alloys: A focused review of mechanical properties and deformation mechanisms, *Acta Mater.* 188 (2020) 435–474.
doi:10.1016/j.actamat.2019.12.015.
- [5] Z. Li, S. Zhao, R.O. Ritchie, M.A. Meyers, Mechanical properties of high-entropy alloys with emphasis on face-centered cubic alloys, *Prog. Mater. Sci.* 102 (2019) 296–345.
doi:10.1016/j.pmatsci.2018.12.003.
- [6] H.Y. Diao, R. Feng, K.A. Dahmen, P.K. Liaw, Fundamental deformation behavior in high-entropy alloys: An overview, *Curr. Opin. Solid State Mater. Sci.* 21 (2017) 252–266.
doi:10.1016/J.COSSMS.2017.08.003.
- [7] J.W. Yeh, S.-K. Chen, S.-J. Lin, J.-Y. Gan, T.-S. Chin, T.-T. Shun, C.-H. Tsau, S.-Y. Chang, Nanostructured High-Entropy Alloys with Multiple Principal Elements: Novel Alloy Design Concepts and Outcomes, *Adv. Eng. Mater.* 6 (2004) 299-303. doi: 10.1002/adem.200300567.
- [8] B. Cantor, I.T.H. Chang, P. Knight, A.J.B. Vincent, Microstructural development in equiatomic multicomponent alloys, *Mater. Sci. Eng. A.* 375–377 (2004) 213–218. doi:10.1016/j.msea.2003.10.257.
- [9] F. Otto, Y. Yang, H. Bei, E.P. George, Relative effects of enthalpy and entropy on the phase stability of equiatomic high-entropy alloys, *Acta Mater.* 61 (2013) 2628–2638.
doi:10.1016/j.actamat.2013.01.042.
- [10] D.B. Miracle, O.N. Senkov, A critical review of high entropy alloys and related concepts, *Acta Mater.* 122 (2017) 448–511. doi:10.1016/j.actamat.2016.08.081.
- [11] O.N. Senkov, D.B. Miracle, K.J. Chaput, J.-P. Couzinie, Development and exploration of refractory high entropy alloys—A review, *J. Mater. Res.* 33 (2018) 1–37. doi:10.1557/jmr.2018.153.
- [12] O.N. Senkov, S. Gorsse, D.B. Miracle, High temperature strength of refractory complex concentrated alloys, *Acta Mater.* 175 (2019) 394–405. doi:10.1016/j.actamat.2019.06.032.
- [13] O.N. Senkov, G.B. Wilks, J.M. Scott, D.B. Miracle, Mechanical properties of Nb₂₅Mo₂₅Ta₂₅W₂₅ and V₂₀Nb₂₀Mo₂₀Ta₂₀W₂₀ refractory high entropy alloys, *Intermetallics.* 19 (2011) 698–706.
doi:10.1016/J.intermet.2011.01.004.
- [14] M. Yang, L. Zhou, C. Wang, P. Jiang, F. Yuan, E. Ma, X. Wu, High impact toughness of CrCoNi medium-entropy alloy at liquid-helium temperature, *Scr. Mater.* 172 (2019) 66–71.
doi:10.1016/j.scriptamat.2019.07.010.
- [15] M. Naeem, H. He, F. Zhang, H. Huang, S. Harjo, T. Kawasaki, B. Wang, S. Lan, Z. Wu, F. Wang, Y. Wu, Z. Lu, Z. Zhang, C.T. Liu, X.-L. Wang, Cooperative deformation in high-entropy alloys at ultralow temperatures, *Sci. Adv.* 6 (2020) eaax4002. doi:10.1126/sciadv.aax4002.
- [16] G. Laplanche, A. Kostka, C. Reinhart, J. Hunfeld, G. Eggeler, E.P. George, Reasons for the superior mechanical properties of medium-entropy CrCoNi compared to high-entropy CrMnFeCoNi, *Acta Mater.* 128 (2017) 292–303. doi:10.1016/j.actamat.2017.02.036.
- [17] Z. Zhang, H. Sheng, Z. Wang, B. Gludovatz, Z. Zhang, E.P. George, Q. Yu, S.X. Mao, R.O. Ritchie, Dislocation mechanisms and 3D twin architectures generate exceptional strength-ductility-

toughness combination in CrCoNi medium-entropy alloy, *Nat. Commun.* 8 (2017) 14390. doi:10.1038/ncomms14390.

- [18] Q. Ding, X. Fu, D. Chen, H. Bei, B. Gludovatz, J. Li, Z. Zhang, E.P. George, Q. Yu, T. Zhu, R.O. Ritchie, Real-time nanoscale observation of deformation mechanisms in CrCoNi-based medium-to high-entropy alloys at cryogenic temperatures, *Mater. Today*. 25 (2019) 21–27. doi:10.1016/j.mattod.2019.03.001.
- [19] P. Chen, C. Lee, S.-Y. Wang, M. Seifi, J.J. Lewandowski, K.A. Dahmen, H. Jia, X. Xie, B. Chen, J.-W. Yeh, C.-W. Tsai, T. Yuan, P.K. Liaw, Fatigue behavior of high-entropy alloys: A review, *Sci. China Technol. Sci.* 61 (2018) 168–178. doi:10.1007/s11431-017-9137-4.
- [20] W. Li, G. Wang, S. Wu, P.K. Liaw, Creep, fatigue, and fracture behavior of high-entropy alloys, *J. Mater. Res.* 33 (2018) 3011–3034. doi:10.1557/jmr.2018.191.
- [21] Z. Chlup, S. Fintová, H. Hadraha, I. Kuběna, M. Vilémová, J. Matějíček, Fatigue behaviour and crack initiation in CoCrFeNiMn high-entropy alloy processed by powder metallurgy, *Metals (Basel)*. 9 (2019) 1110. doi:10.3390/met9101110.
- [22] M.A. Hemphill, T. Yuan, G.Y. Wang, J.W. Yeh, C.W. Tsai, A. Chuang, P.K. Liaw, Fatigue behavior of $\text{Al}_{0.5}\text{CoCrCuFeNi}$ high entropy alloys, *Acta Mater.* 60 (2012) 5723–5734. doi:10.1016/j.actamat.2012.06.046.
- [23] K. Liu, S.S. Nene, M. Frank, S. Sinha, R.S. Mishra, Extremely high fatigue resistance in an ultrafine grained high entropy alloy, *Appl. Mater. Today*. 15 (2019) 525–530. doi:10.1016/j.apmt.2019.04.001.
- [24] K. Lu, A. Chauhan, D. Litvinov, M. Walter, A.S. Tirunilai, J. Freudenberg, A. Kauffmann, M. Heilmaier, J. Aktaa, High-temperature low cycle fatigue behavior of an equiatomic CoCrFeMnNi high-entropy alloy, *Mater. Sci. Eng. A*. 791 (2020) 139781. doi:10.1016/j.msea.2020.139781.
- [25] M. Seifi, D. Li, Z. Yong, P.K. Liaw, J.J. Lewandowski, Fracture toughness and fatigue crack growth behavior of as-cast high-entropy alloys, *JOM*. 67 (2015) 2288–2295. doi:10.1007/s11837-015-1563-9.
- [26] Z. Tang, T. Yuan, C.-W. Tsai, J.-W. Yeh, C.D. Lundin, P.K. Liaw, Fatigue behavior of a wrought $\text{Al}_{0.5}\text{CoCrCuFeNi}$ two-phase high-entropy alloy, *Acta Mater.* 99 (2015) 247–258. doi:10.1016/j.actamat.2015.07.004.
- [27] K. Alagarsamy, A. Fortier, M. Komarasamy, N. Kumar, A. Mohammad, S. Banerjee, H.-C. Han, R.S. Mishra, Mechanical properties of high entropy alloy $\text{Al}_{0.1}\text{CoCrFeNi}$ for peripheral vascular stent application, *Cardiovasc. Eng. Technol.* 7 (2016) 448–454. doi:10.1007/s13239-016-0286-6.
- [28] K.V.S. Thurston, B. Gludovatz, A. Hohenwarter, G. Laplanche, E.P. George, R.O. Ritchie, Effect of temperature on the fatigue-crack growth behavior of the high-entropy alloy CrMnFeCoNi, *Intermetallics*. 88 (2017) 65–72. doi:10.1016/j.intermet.2017.05.009.
- [29] K. Suzuki, M. Koyama, H. Noguchi, Small fatigue crack growth in a high entropy alloy, *Procedia Struct. Integr.* 13 (2018) 1065–1070. doi:10.1016/j.prostr.2018.12.224.
- [30] B. Guennec, V. Kentheswaran, L. Perrière, A. Ueno, I. Guillot, J.-P. Couzinié, G. Dirras, Four-point bending fatigue behavior of an equimolar BCC HfNbTaTiZr high-entropy alloy: Macroscopic and microscopic viewpoints, *Materialia*. 4 (2018) 348–360. doi:10.1016/j.mtla.2018.09.040.
- [31] T. Niendorf, T. Wegener, Z. Li, D. Raabe, Unexpected cyclic stress-strain response of dual-phase

- high-entropy alloys induced by partial reversibility of deformation, *Scr. Mater.* 143 (2018) 63–67. doi:10.1016/j.scriptamat.2017.09.013.
- [32] S. Shukla, T. Wang, S. Cotton, R.S. Mishra, Hierarchical microstructure for improved fatigue properties in a eutectic high entropy alloy, *Scr. Mater.* 156 (2018) 105–109. doi:10.1016/j.scriptamat.2018.07.022.
- [33] K.V.S. Thurston, B. Gludovatz, Q. Yu, G. Laplanche, E.P. George, R.O. Ritchie, Temperature and load-ratio dependent fatigue-crack growth in the CrMnFeCoNi high-entropy alloy, *J. Alloys Compd.* (2019). doi:10.1016/j.jallcom.2019.04.234.
- [34] N. Kashaev, V. Ventzke, N. Petrov, M. Horstmann, S. Zherebtsov, D. Shaysultanov, V. Sanin, N. Stepanov, Fatigue behaviour of a laser beam welded CoCrFeNiMn-type high entropy alloy, *Mater. Sci. Eng. A.* 766 (2019) 138358. doi:10.1016/j.msea.2019.138358.
- [35] K. Liu, M. Komarasamy, B. Gwalani, S. Shukla, R.S. Mishra, Fatigue behavior of ultrafine grained triplex Al_{0.3}CoCrFeNi high entropy alloy, *Scr. Mater.* 158 (2019) 116–120. doi:10.1016/j.scriptamat.2018.08.048.
- [36] K. Liu, B. Gwalani, M. Komarasamy, S. Shukla, T. Wang, R.S. Mishra, Effect of nano-sized precipitates on the fatigue property of a lamellar structured high entropy alloy, *Mater. Sci. Eng. A.* 760 (2019) 225–230. doi:10.1016/j.msea.2019.06.012.
- [37] W. Li, X. Long, S. Huang, Q. Fang, C. Jiang, Elevated fatigue crack growth resistance of Mo alloyed CoCrFeNi high entropy alloys, *Eng. Fract. Mech.* 218 (2019) 106579. doi:10.1016/j.engfracmech.2019.106579.
- [38] B. Guennec, V. Kentheswaran, L. Perrière, A. Ueno, I. Guillot, J.-P. Couzinié, G. Dirras, Analysis of the fatigue crack growth mechanisms in equimolar body centered cubic HfNbTaTiZr high-entropy alloy: Discussions on its singularities and consequences on the crack propagation rate properties, *Intermetallics*. 110 (2019) 106459. doi:10.1016/j.intermet.2019.04.002.
- [39] Y.-K. Kim, G.-S. Ham, H.S. Kim, K.-A. Lee, High-cycle fatigue and tensile deformation behaviors of coarse-grained equiatomic CoCrFeMnNi high entropy alloy and unexpected hardening behavior during cyclic loading, *Intermetallics*. 111 (2019) 106486. doi:10.1016/j.intermet.2019.106486.
- [40] Y.Z. Tian, S.J. Sun, H.R. Lin, Z.F. Zhang, Fatigue behavior of CoCrFeMnNi high-entropy alloy under fully reversed cyclic deformation, *J. Mater. Sci. Technol.* 35 (2019) 334–340. doi:10.1016/j.jmst.2018.09.068.
- [41] C. J. Gilbert, J. M. McNaney, R. H. Dauskardt, R. O. Ritchie, Back-face strain compliance and electrical-potential crack length calibrations for the disk-shaped compact-tension DC(T) specimen, *J. Test. Eval.* 22 (2009) 117–120. doi:10.1520/jte12644j.
- [42] ASTM E647, Standard Test Method for Measurement of Fatigue Crack Growth Rates, Am. Soc. Test. Mater. (2014) 1–50. doi:10.1520/E0647-13A.2.
- [43] W. Elber, Fatigue crack closure under cyclic tension. *Eng. Fract. Mech.* 2 (1970) 37–44. doi:10.1016/0013-7944(70)90028-7
- [44] R. Pippan, A. Hohenwarter, Fatigue crack closure: A review of the physical phenomena, *Fatigue Fract. Eng. Mater. Struct.* 40 (2017) 471–495. doi:10.1111/ffe.12578.

- [45] J.E. Allison, R.C. Ku, M.E. Pompetski, A comparison of measurement methods and numerical procedures for the experimental characterization of fatigue crack closure, in Mechanics of Fatigue Crack Closure, eds. J.C. Newman and W. Elber, ASTM STP 982, ASTM Intl., West Conshohocken, PA: (1988), pp. 171-185. doi:10.1520/stp27207s.
- [46] R.O. Ritchie, Near-threshold fatigue-crack propagation in steels, *Int. Met. Rev.* 24 (1979) 205–230. doi:10.1179/imtr.1979.24.1.205.
- [47] J.L. Robinson, C.J. Beevers, The effects of load ratio, interstitial content, and grain size on low-stress fatigue-crack propagation in α -titanium, *Met. Sci. J.* 7 (1973) 153–159. doi:10.1179/030634573790445550.
- [48] S. Suresh, R.O. Ritchie, Geometric model for fatigue crack closure induced by fracture surface roughness., *Metall. Trans A.* 13A (1982) 1627–1631. doi:10.1007/bf02644803.
- [49] R.O. Ritchie, Mechanisms of fatigue crack propagation in metals, ceramics and composites: Role of crack tip shielding, *Mater. Sci. Eng. A.* 103 (1988) 15–28. doi:10.1016/0025-5416(88)90547-2.
- [50] R.A. Schmidt, P.C. Paris, Threshold for fatigue crack propagation and the effects of load ratio and frequency, in Progress in Flaw Growth and Fracture Toughness Testing, ASTM STP 536, ASTM Intl., West Conshohocken, PA: (1973), pp. 79–94. doi:10.1520/stp49638s.
- [51] R. Pippan, K. Haberz, H.P. Stüwe, The plastic deformation of fracture surface contacts in fatigue, *Eng. Fract. Mech.* 53 (1996) 441–448. doi:10.1016/0013-7944(95)00114-X.
- [52] G. Laplanche, A. Kostka, O.M. Horst, G. Eggeler, E.P. George, Microstructure evolution and critical stress for twinning in the CrMnFeCoNi high-entropy alloy, *Acta Mater.* 118 (2016) 152–163. doi:10.1016/j.actamat.2016.07.038.
- [53] K.V.S. Thurston, A. Hohenwarter, G. Laplanche, E.P. George, B. Gludovatz, R.O. Ritchie, On the onset of deformation twinning in the CrFeMnCoNi high-entropy alloy using a novel tensile specimen geometry, *Intermetallics.* 110 (2019) 106469. doi:10.1016/j.intermet.2019.04.012.
- [54] T. Niendorf, F. Rubitschek, H.J. Maier, J. Niendorf, H.A. Richard, A. Frehn, Fatigue crack growth—Microstructure relationships in a high-manganese austenitic TWIP steel, *Mater. Sci. Eng. A.* 527 (2010) 2412–2417. doi:10.1016/j.msea.2009.12.012.
- [55] M. Clavel, A. Pineau, Fatigue behaviour of two nickel-base alloys I: Experimental results on low cycle fatigue, fatigue crack propagation and substructures, *Mater. Sci. Eng.* 55 (1982) 157–171. doi:10.1016/0025-5416(82)90129-X.
- [56] J.L. Yuen, P. Roy, Effect of grain size on the near threshold fatigue crack propagation of a nickel base precipitation hardened superalloy, *Scr. Metall.* 19 (1985) 17–22. doi:10.1016/0036-9748(85)90257-1.
- [57] J.E. King, Fatigue crack propagation in nickel-base superalloys – effects of microstructure, load ratio, and temperature, *Mater. Sci. Technol.* 3 (1987) 750–764. doi:10.1179/mst.1987.3.9.750.

Table 1. Uniaxial tensile properties of the CrCoNi alloy with coarse (68 μm) and fine (7 μm) grain sizes tested at temperatures of 293K, 198K and 77K.

Grain size (μm)	Temperature (K)	Yield strength σ_y (MPa)	Tensile strength σ_{uts} (MPa)	Uniform elongation ε_{ue}	Strain to failure ε_f
7	293	524 \pm 9	889 \pm 13	33.3 \pm 1.5%	43.3 \pm 4.0%
	198	580 \pm 23	1024 \pm 36	40.5 \pm 2.1%	49.5 \pm 3.5%
	77	728 \pm 6	1290 \pm 2	51.0 \pm 1.4%	58.0 \pm 2.8%
68	293	289 \pm 21	777 \pm 5	59.0 \pm 1.4%	70.5 \pm 0.7%
	198	337 \pm 42	886 \pm 16	66.0 \pm 2.8%	77.5 \pm 3.5%
	77	486 \pm 1	1120 \pm 10	72.0 \pm 1.4%	79.0 \pm 2.8%

Table 2. Experimental results for the fatigue-crack propagation behavior of the CrCoNi alloy with coarse (68 μm) and fine (7 μm) grain sizes tested at temperatures of 293K, 198K and 77K at a load ratio of $R = 0.1$.

Grain size (μm)	Temperature (K)	Yield strength σ_y (MPa)	Paris exponent m	ΔK_{th} (MPa $\sqrt{\text{m}}$)	$\Delta K_{\text{th,eff}}^*$ (MPa $\sqrt{\text{m}}$)
7	293	524 \pm 9	3.3	5.7	3.0
	198	580 \pm 23	3.3	7	4.8
	77	728 \pm 6	2.7	8	4.9
68	293	289 \pm 21	3.9	9.4	4.3
	198	337 \pm 42	3.8	11	6.5
	77	486 \pm 1	3	13.7	9.0

* $\Delta K_{\text{th,eff}}$ is the effective threshold stress-intensity range defined as $\Delta K_{\text{th,eff}} = K_{\text{th,max}} - K_{\text{th,cl}}$ where $K_{\text{th,max}}$ and $K_{\text{th,cl}}$ are the maximum and approximate closure stress intensity at the fatigue threshold, respectively.

Table 3. Comparison of the fatigue-crack growth results for the CrCoNi MEA and CrMnFeCoNi HEA with comparable structural materials, at room temperature with $R = 0.1$.

Alloy	Grain size (μm)	Yield strength (MPa)	Tensile strength (MPa)	Fatigue threshold ΔK_{th} (MPa $\sqrt{\text{m}}$)	Paris exponent m
CrCoNi	7	430	889	5.7	3.3
CrCoNi	68	289	777	9.4	3.9
CrMnFeCoNi [1,28]	7	410	780	4.8	3.5
Waspaloy [55,57]	100	860	1310	~12	4.6
Inconel [56]	22	1073	1349	7.9	3.4
XIP 1000 TWIP steel [54]	2	580	1160	5.9	2.7
300-M steel* [46]	20	1700	n/a	3.1	2.5
Fe-4Cr-0.35C steel* [46]	30	1300	n/a	4.4	2.6

*300-M steel and Fe-4Cr-0.35C steel were fatigue tested at R -ratio of 0.05 at room temperature [46].

List of Figure Captions

Fig. 1. Schematic showing the determination of the closure load (P_{cl}): by finding the intersection point of two straight lines fitted to the elastic compliance (or load *vs.* back-face strain) curve near the ends of P_{max} and P_{min} , respectively, during a typical unloading cycle.

Fig. 2. Microstructure and tensile properties of the fine-grained and coarse-grained CrCoNi alloy. Inverse pole figure (IPF) maps of the cross-sections of the swaged rods show uniform equiaxed grains with sizes of (a) $\sim 7 \mu\text{m}$ after recrystallization at 1073K for 1h and (b) $\sim 68 \mu\text{m}$ after a further anneal of 1 h at 1173K. Representative engineering stress-strain curves for the (c) $\sim 7 \mu\text{m}$ and (d) $\sim 68 \mu\text{m}$ grain-size structures, measured at 293K, 198K and 77K, showing increases in yield strength, tensile strength, and strain to failure as the temperature is decreased from room temperature to cryogenic temperatures of 198K and 77K.

Fig. 3. Fatigue-crack propagation behavior for the CrCoNi alloy with two different grain sizes of $7 \mu\text{m}$ and $68 \mu\text{m}$ tested at temperatures of 293K, 198K and 77K. The threshold stress-intensity range (ΔK_{th}) for the fine-grained alloy increased by 40% from $\Delta K_{th} \sim 5.7 \text{ MPa}\sqrt{\text{m}}$ at room temperature to $\Delta K_{th} \sim 8 \text{ MPa}\sqrt{\text{m}}$ at 77K. Even higher ΔK_{th} thresholds were measured in the coarse-grained alloy, from $\Delta K_{th} \sim 9.4 \text{ MPa}\sqrt{\text{m}}$ at 293K to $\sim 13.7 \text{ MPa}\sqrt{\text{m}}$ at 77K. The arrow at the left indicates a crack growth rate of approximately one lattice spacing per cycle.

Fig. 4. The threshold stress-intensity range ΔK_{th} in the coarse- and fine-grained CrCoNi MEA as a function of the yield strength for $R = 0.1$. Although threshold values are overall higher in the coarse-grained microstructures as compared to those in the fine-grained material, there is a linear correlation between ΔK_{th} and the temperature-dependent yield strength for CrCoNi for a specific grain size. The same linear trend is found for the CrMnFeCoNi Cantor HEA with a similar grain size to the CrCoNi MEA [28].

Fig. 5. Variation of the magnitude of crack closure, in terms of the ratio of closure stress intensity to the maximum stress intensity (K_{cl}/K_{max}), as a function of the stress-intensity range (ΔK). The coarse-grained microstructure displays higher overall levels of crack closure which is ascribed to the rougher fracture surfaces in the larger-grained material. Closure levels progressively increase in the near-threshold regime as ΔK_{th} is approached; this can be attributed to enhanced roughness-induced crack closure due to the rougher fracture surfaces, and the smaller crack-opening displacements, which scale with K^2 , as the stress-intensity range is reduced.

Fig. 6. Fatigue-crack propagation behavior of the fine- and coarse-grained CrCoNi MEA plotted in terms of da/dN vs. ΔK and ΔK_{eff} (a) da/dN vs. ΔK_{eff} curves, where $\Delta K_{\text{eff}} = K_{\max} - K_{\text{cl}}$ (when $K_{\text{cl}} > K_{\min}$), for all grain sizes and temperatures. Comparison of the da/dN vs. ΔK_{eff} and da/dN vs. ΔK curves, at (b) 293K, (c) 198K, and (d) 77K. Whereas in the mid-range of growth rates, the da/dN vs. ΔK_{eff} and ΔK curves converge into a narrow band as the role of crack closure is relatively minor, with decreasing growth rates into the near-threshold regime the role of crack closure and its effect on the local stress-intensity range actually experienced at the crack tip becomes far more significant. However, there still remains a difference between the da/dN vs. ΔK_{eff} curves for the two grain sizes in this regime that cannot be fully accounted for in terms of the measured crack closure levels.

Fig. 7. EBSD scans of near-threshold fatigue crack path profiles in the fine- and coarse-grained CrCoNi structures at 293K, 198K and 77K. (a) Crack propagation in the fine-grained alloy is transgranular at 293K, with the crack traversing the grains and annealing twins. Due to the relatively low yield strength at 293K, significant plastic deformation in the plastic wake can slightly flatten the crack flanks, leading to a loss of crack-tip shielding and hence fatigue resistance. (b) Mixed intergranular and transgranular fracture at 198K, the intergranular crack path inducing a higher degree of roughness-induced crack closure. (c) Crack propagation in the fine-grained alloy at 77K is largely transgranular, although the crack path is frequently deflected by profuse deformation-induced nano-twins nucleated by the high stresses near the crack tip. The resultant local deviation in crack path at the sub-grain and nano-twin length-scales acts to enhance crack closure, thereby raising the ΔK_{th} threshold. (d) A transgranular mode is also in evidence in the coarse-grained microstructure at 293K, where the increased density of recrystallization twins during annealing leads to frequent crack deflection within the large grains. (e) Mixed intergranular and transgranular fracture in the coarse-grained structure at 198K. (f) Crack propagation in the coarse-grained alloy at 77K. Note that nano-twinning is not activated in the 68 μm structure in the near-threshold regime.

Fig. 8. EBSD scans of the tortuous fatigue crack path profiles, specifically showing frequent crack deflections caused by encounters with deformation twins, in the (a) fine-grained alloy in the near-threshold regime close to $\Delta K_{\text{th}} \sim 8 \text{ MPa}\sqrt{\text{m}}$, at 77K, and (b) coarse-grained alloy at a higher $\Delta K \sim 28 \text{ MPa}\sqrt{\text{m}}$, also at 77K.

Fig. 9. SEM images of the fatigue fractography of the fine- and coarse-grained CrCoNi structures in the near-threshold regime at 293K, 198K and 77K. The fracture surfaces in the (a) fine-grained and (b) coarse-grained alloys are transgranular at 293K and display serrations with sharp edges resulting from crack-tip blunting and resharpening due to cyclic plasticity. At

198K, the fracture morphology in the (c) fine-grained and (d) coarse-grained alloys is similar to the fine-grained alloy with a mixture of transgranular fracture and intergranular fracture, although the coarser grain size confers higher surface roughness, which promotes crack closure. (e) At 77K, the fracture surface of the fine-grained alloy is mainly transgranular with minor intergranular features. Due to the operation of nano-twinning at 77K, the nano-twins lead to local crack deflection and hence a rougher fracture surface. (f) At 77K, the corresponding fracture surface in the coarse-grained alloy shows a markedly rough morphology comprising serrations with sharp edges oriented in more than one direction, which likely result from multiple cyclic planar slip. The vertical arrows represent the general direction of crack growth.

Fig. 10. TEM characterization of the nano-twins and dislocations in the plastic wake within 12 μm of the fatigue fracture surface. Deformation nano-twins are absent in the plastic wake in the fine-grained alloy in the near-threshold regime (a) at 293K and (b) 198K, but are evident (c) at 77K. (d) In the coarse-grained alloy tested in the near-threshold regime at 77K, nano-twins are not observed; however, profuse stacking faults and planar slip bands can be readily seen. (e) Twin-twin network formed by deformation nano-twins with multiple variants can be seen in the coarse-grained alloy tested at a higher $\Delta K \sim 28 \text{ MPa}\sqrt{\text{m}}$ at 77K. Note that the twin lamella shown in (b) are annealing twins rather than deformation twins.

Fig. 11. Comparison of the crack-propagation fatigue behavior of the CrCoNi MEA with the CrMnFeCoNi high-entropy alloy and several other comparable structural alloys: specifically, austenitic stainless steels [46], twinning-induced plasticity (TWIP) steels [54], and nickel-based superalloys [55–57].

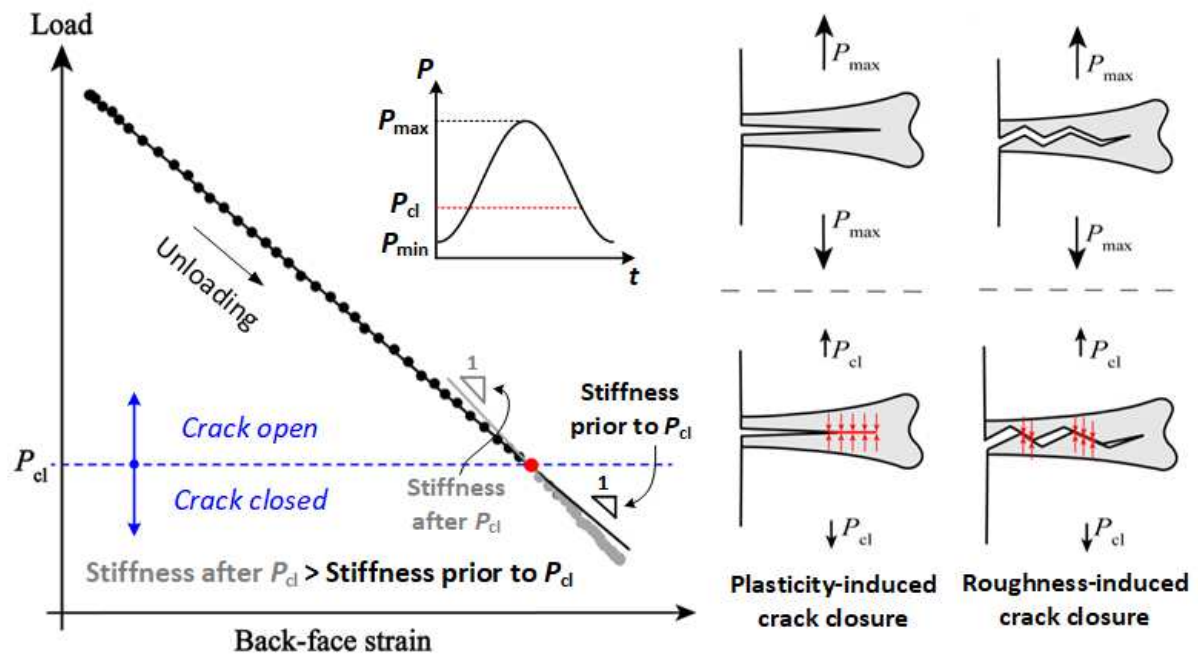


Fig. 1. Schematic showing the determination of the closure load (P_{cl}): by finding the intersection point of two straight lines fitted to the elastic compliance (or load vs. back-face strain) curve near the ends of P_{max} and P_{min} , respectively, during a typical unloading cycle.

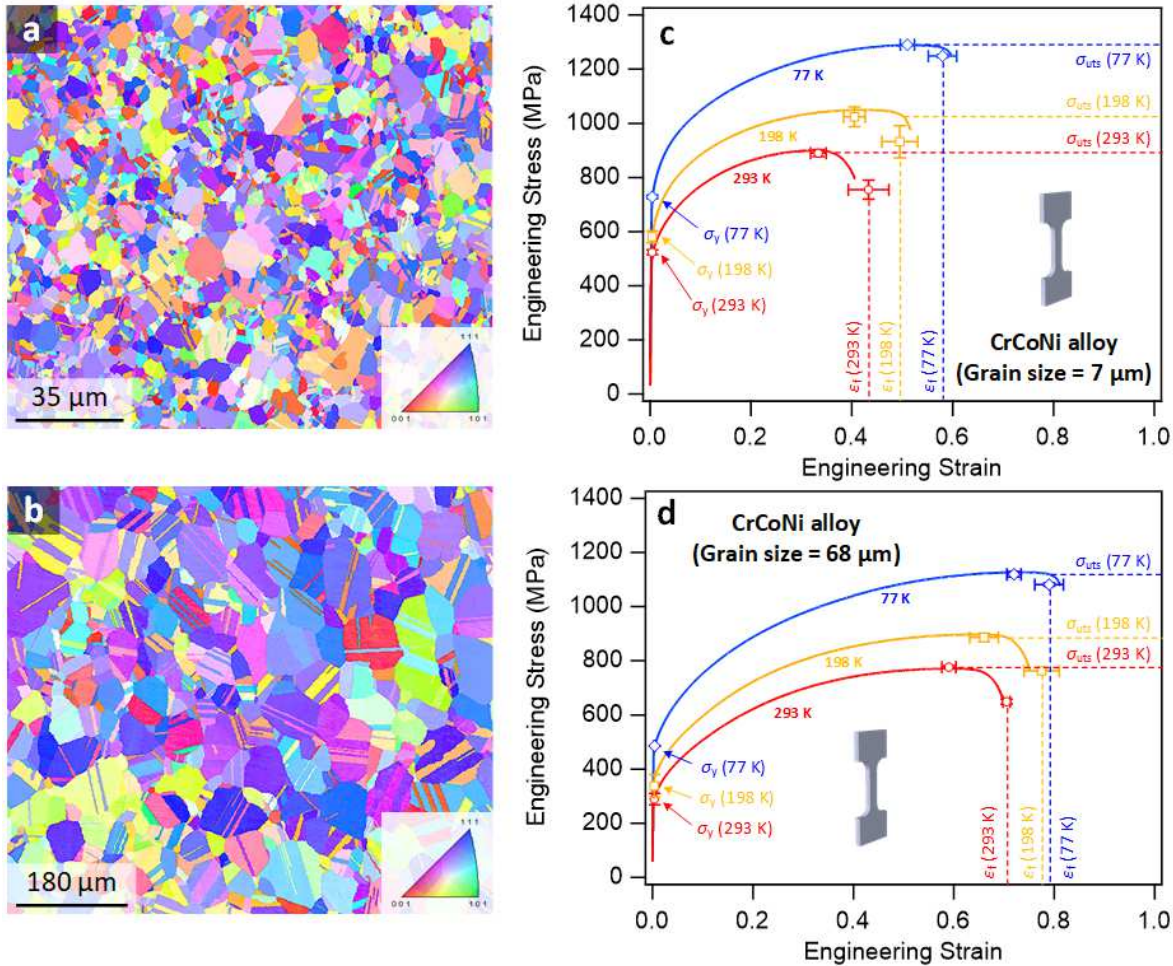


Fig. 2. Microstructure and tensile properties of the fine-grained and coarse-grained CrCoNi alloy. Inverse pole figure (IPF) maps of the cross-sections of the swaged rods show uniform equiaxed grains with sizes of (a) $\sim 7 \mu\text{m}$ after recrystallization at 1073K for 1h and (b) $\sim 68 \mu\text{m}$ after a further anneal of 1 h at 1173K. Representative engineering stress-strain curves for the (c) $\sim 7 \mu\text{m}$ and (d) $\sim 68 \mu\text{m}$ grain-size structures, measured at 293K, 198K and 77K, showing increases in yield strength, tensile strength, and strain to failure as the temperature is decreased from room temperature to cryogenic temperatures of 198K and 77K.

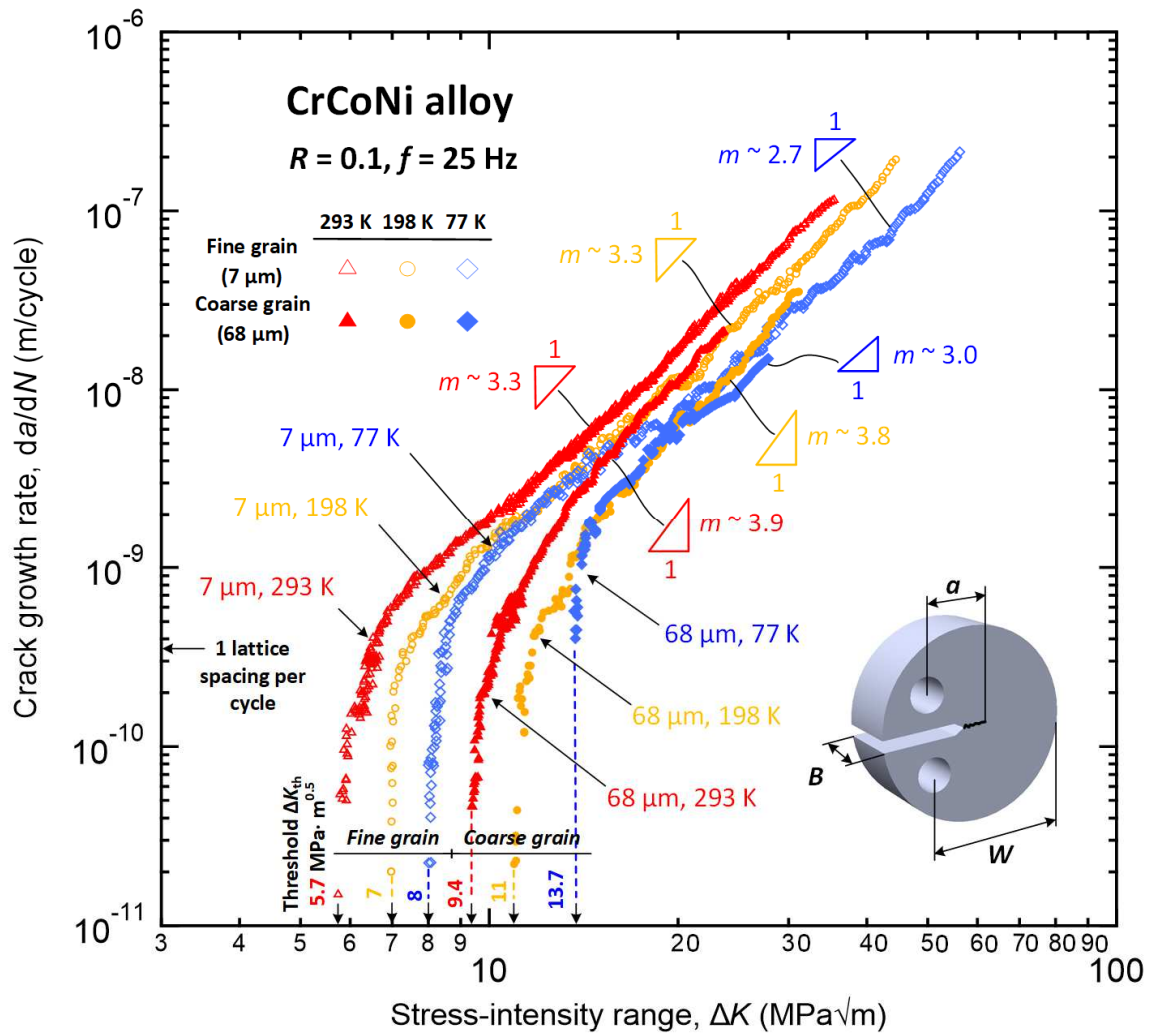


Fig. 3. Fatigue-crack propagation behavior for the CrCoNi alloy with two different grain sizes of 7 μm and 68 μm tested at temperatures of 293K, 198K and 77K. The threshold stress-intensity range (ΔK_{th}) for the fine-grained alloy increased by 40% from $\Delta K_{\text{th}} \sim 5.7 \text{ MPa}\sqrt{\text{m}}$ at room temperature to $\Delta K_{\text{th}} \sim 8 \text{ MPa}\sqrt{\text{m}}$ at 77K. Even higher ΔK_{th} thresholds were measured in the coarse-grained alloy, from $\Delta K_{\text{th}} \sim 9.4 \text{ MPa}\sqrt{\text{m}}$ at 293K to $\sim 13.7 \text{ MPa}\sqrt{\text{m}}$ at 77K. The arrow at the left indicates a crack growth rate of approximately one lattice spacing per cycle.

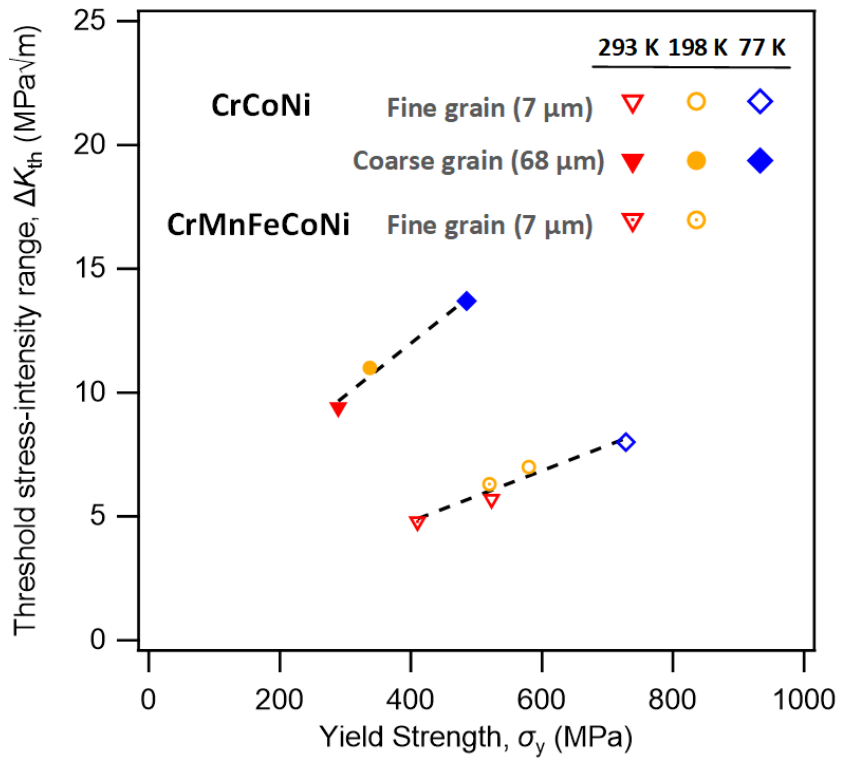


Fig. 4. The threshold stress-intensity range ΔK_{th} in the coarse- and fine-grained CrCoNi MEA as a function of the yield strength for $R = 0.1$. Although threshold values are overall higher in the coarse-grained microstructures as compared to those in the fine-grained material, there is a linear correlation between ΔK_{th} and the temperature-dependent yield strength for CrCoNi for a specific grain size. The same linear trend is found for the CrMnFeCoNi Cantor HEA with a similar grain size to the CrCoNi MEA [28].

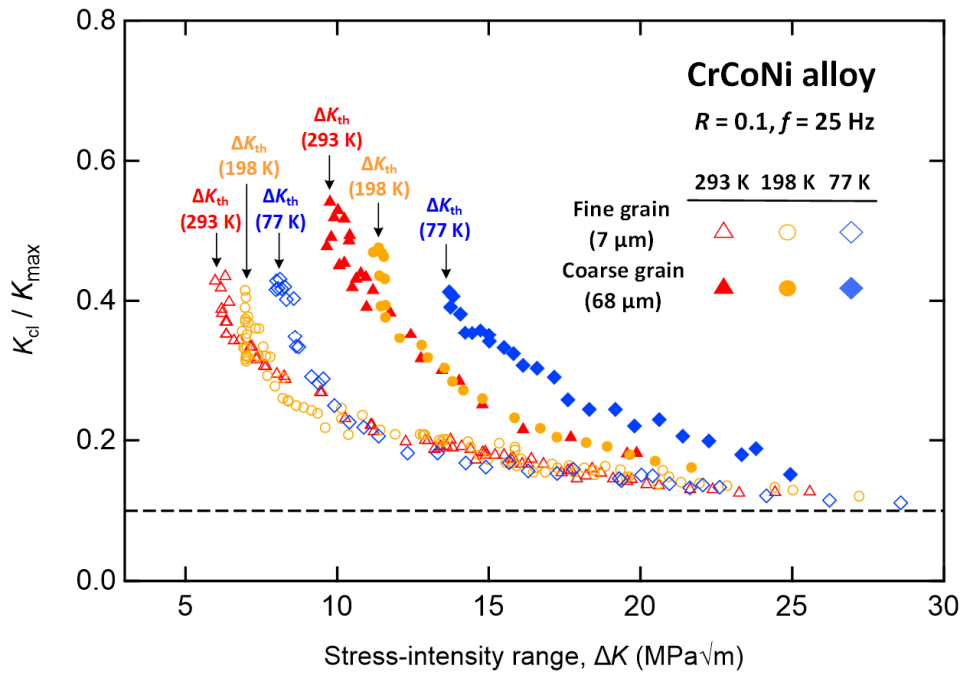


Fig. 5. Variation of the magnitude of crack closure, in terms of the ratio of closure stress intensity to the maximum stress intensity ($K_{\text{cl}}/K_{\text{max}}$), as a function of the stress-intensity range (ΔK). The coarse-grained microstructure displays higher overall levels of crack closure which is ascribed to the rougher fracture surfaces in the larger-grained material. Closure levels progressively increase in the near-threshold regime as ΔK_{th} is approached; this can be attributed to enhanced roughness-induced crack closure due to the rougher fracture surfaces, and the smaller crack-opening displacements, which scale with K^2 , as the stress-intensity range is reduced.

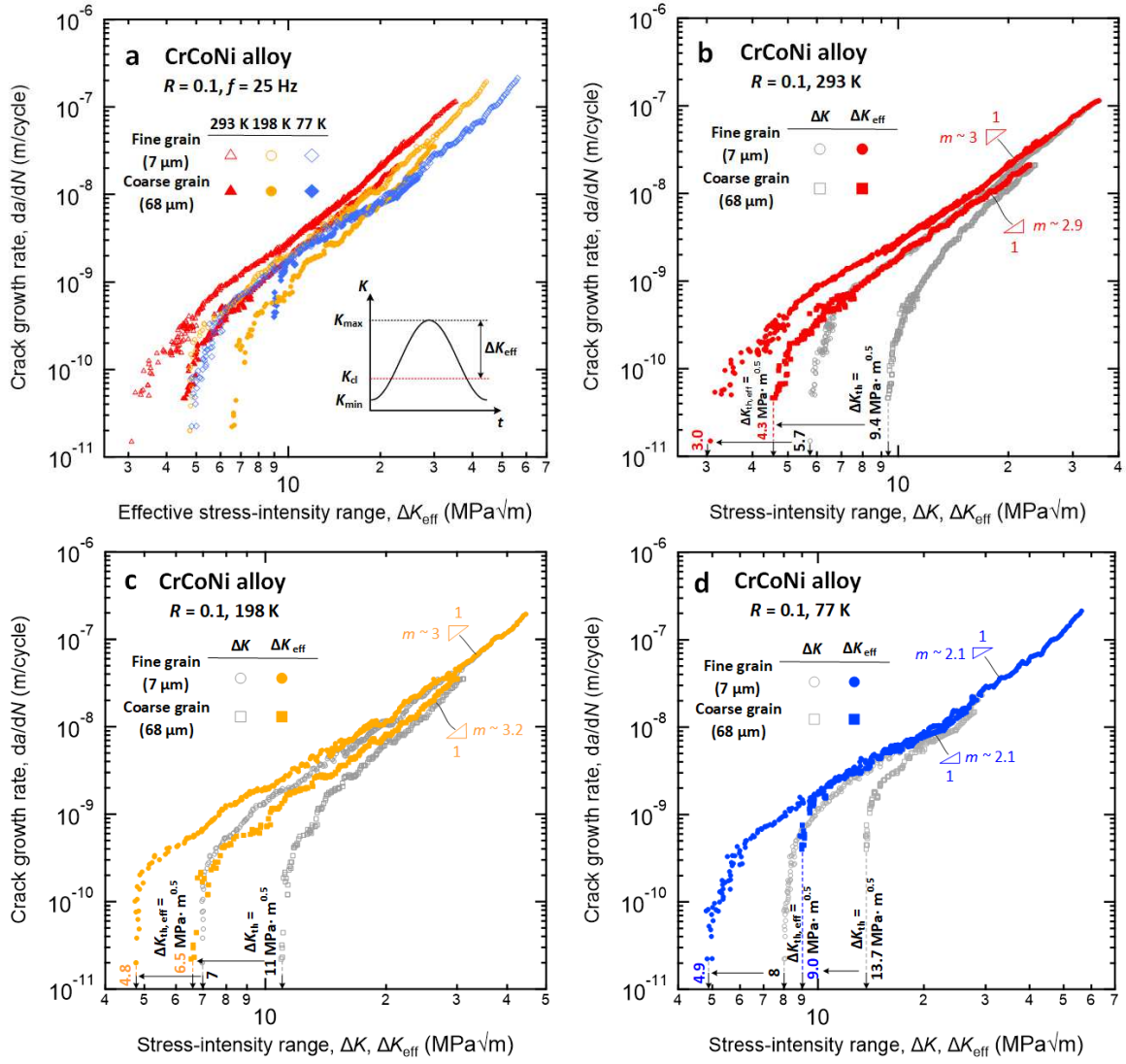


Fig. 6. Fatigue-crack propagation behavior of the fine- and coarse-grained CrCoNi MEA plotted in terms of da/dN vs. ΔK and ΔK_{eff} (a) da/dN vs. ΔK_{eff} curves, where $\Delta K_{\text{eff}} = K_{\max} - K_{\text{cl}}$ (when $K_{\text{cl}} > K_{\min}$), for all grain sizes and temperatures. Comparison of the da/dN vs. ΔK_{eff} and da/dN vs. ΔK curves, at (b) 293 K, (c) 198 K, and (d) 77 K. Whereas in the mid-range of growth rates, the da/dN vs. ΔK_{eff} and da/dN vs. ΔK curves converge into a narrow band as the role of crack closure is relatively minor, with decreasing growth rates into the near-threshold regime the role of crack closure and its effect on the local stress-intensity range actually experienced at the crack tip becomes far more significant. However, there still remains a difference between the da/dN vs. ΔK_{eff} curves for the two grain sizes in this regime that cannot be fully accounted for in terms of the measured crack closure levels.

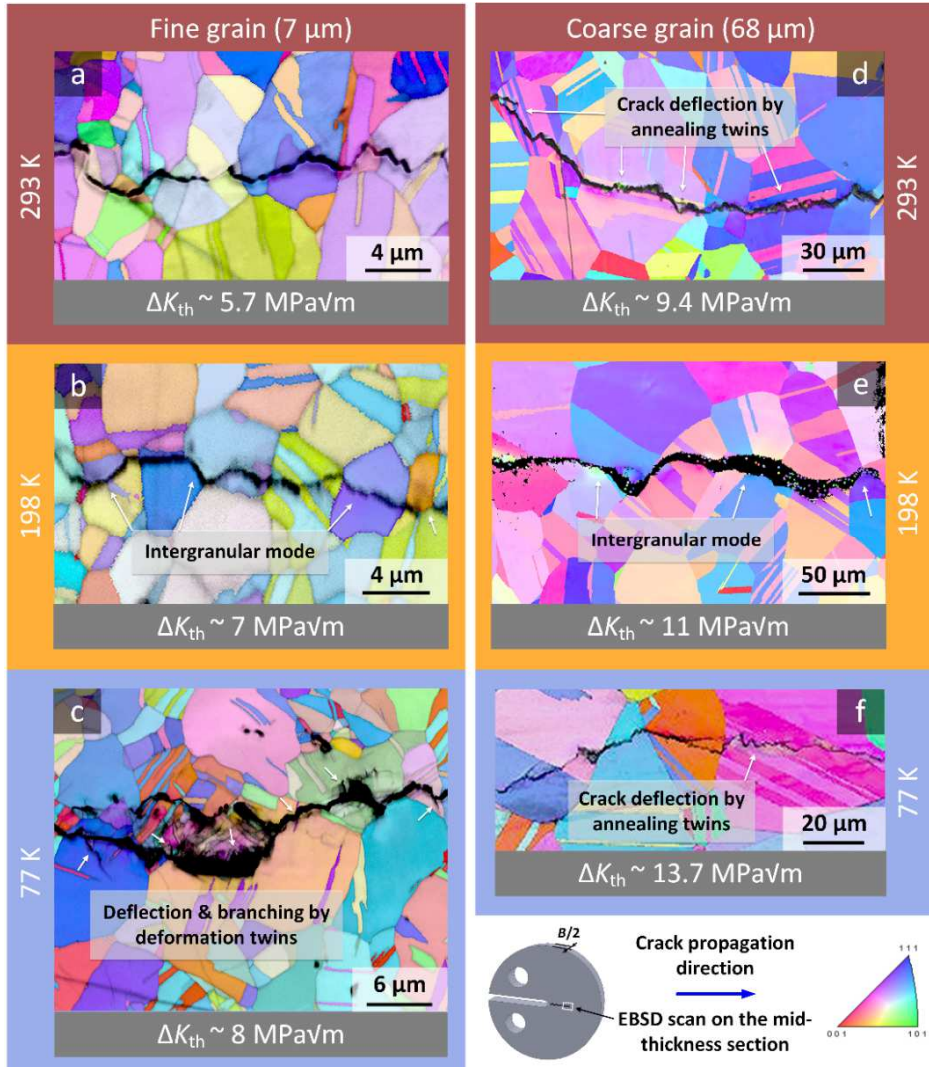


Fig. 7. EBSD scans of near-threshold fatigue crack path profiles in the fine- and coarse-grained CrCoNi structures at 293K, 198K and 77K. (a) Crack propagation in the fine-grained alloy is transgranular at 293K, with the crack traversing the grains and annealing twins. Due to the relatively low yield strength at 293K, significant plastic deformation in the plastic wake can slightly flatten the crack flanks, leading to a loss of crack-tip shielding and hence fatigue resistance. (b) Mixed intergranular and transgranular fracture at 198K, the intergranular crack path inducing a higher degree of roughness-induced crack closure. (c) Crack propagation in the fine-grained alloy at 77K is largely transgranular, although the crack path is frequently deflected by profuse deformation-induced nano-twins nucleated by the high stresses near the crack tip. The resultant local deviation in crack path at the sub-grain and nano-twin length-scales acts to enhance crack closure, thereby raising the ΔK_{th} threshold. (d) A transgranular mode is also in evidence in the coarse-grained microstructure at 293K, where the increased density of recrystallization twins during annealing leads to frequent crack deflection within the large grains. (e) Mixed intergranular and transgranular fracture in the coarse-grained structure at 198K. (f) Crack

propagation in the coarse-grained alloy at 77K. Note that nano-twinning is not activated in the 68 μm structure in the near-threshold regime.

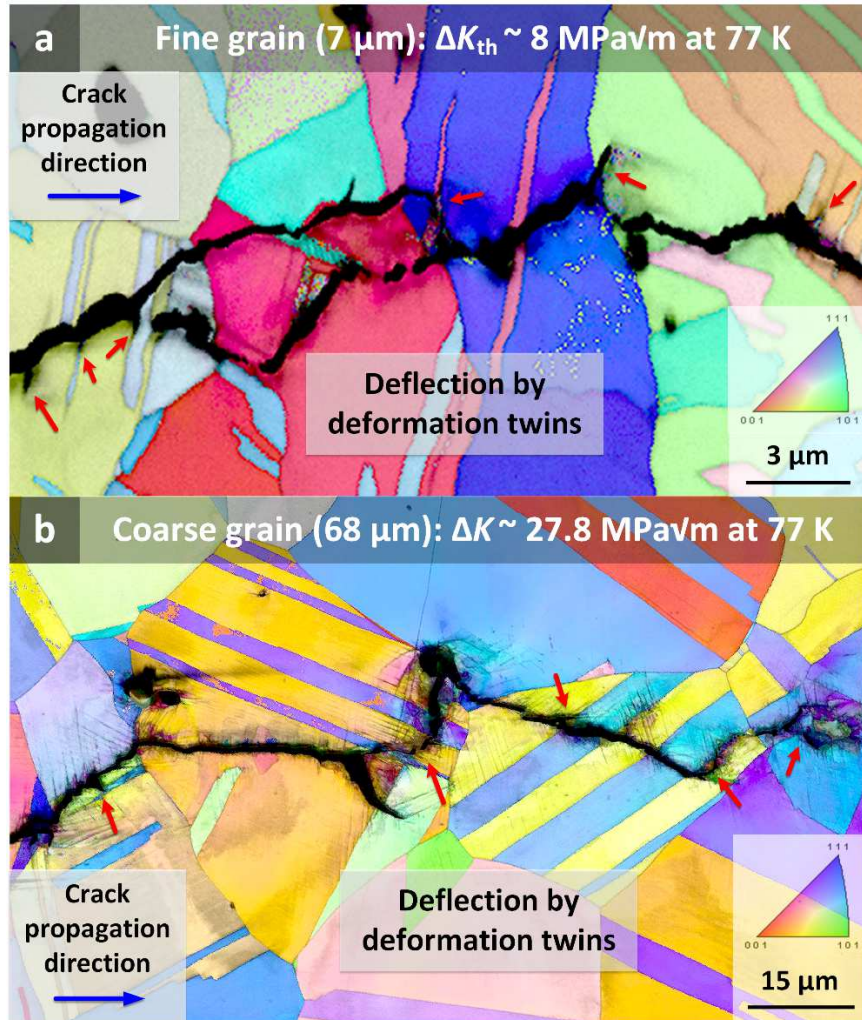


Fig. 8. EBSD scans of the tortuous fatigue crack path profiles, specifically showing frequent crack deflections caused by encounters with deformation twins, in the (a) fine-grained alloy in the near-threshold regime close to $\Delta K_{\text{th}} \sim 8 \text{ MPa}\sqrt{\text{m}}$, at 77K, and (b) coarse-grained alloy at a higher $\Delta K \sim 28 \text{ MPa}\sqrt{\text{m}}$, also at 77K.

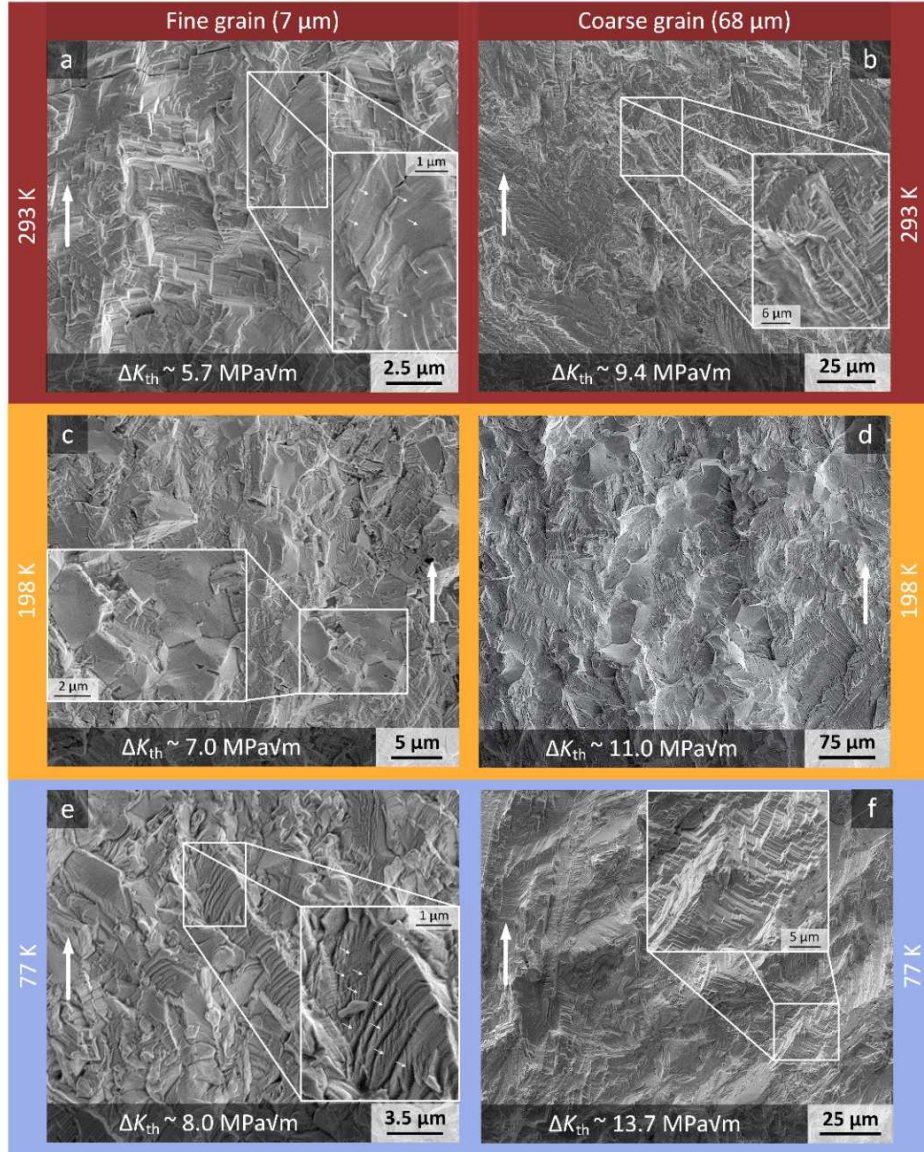


Fig. 9. SEM images of the fatigue fractography of the fine- and coarse-grained CrCoNi structures in the near-threshold regime at 293K, 198K and 77K. The fracture surfaces in the (a) fine-grained and (b) coarse-grained alloys are transgranular at 293K and display serrations with sharp edges resulting from crack-tip blunting and resharpening due to cyclic plasticity. At 198K, the fracture morphology in the (c) fine-grained and (d) coarse-grained alloys is similar to the fine-gained alloy with a mixture of transgranular fracture and intergranular fracture, although the coarser grain size confers higher surface roughness, which promotes crack closure. (e) At 77K, the fracture surface of the fine-grained alloy is mainly transgranular with minor intergranular features. Due to the operation of nano-twinning at 77K, the nano-twins lead to local crack deflection and hence a rougher fracture surface. (f) At 77K, the

corresponding fracture surface in the coarse-grained alloy shows a markedly rough morphology comprising serrations with sharp edges oriented in more than one direction, which likely result from multiple cyclic planar slip. The vertical arrows represent the general direction of crack growth.

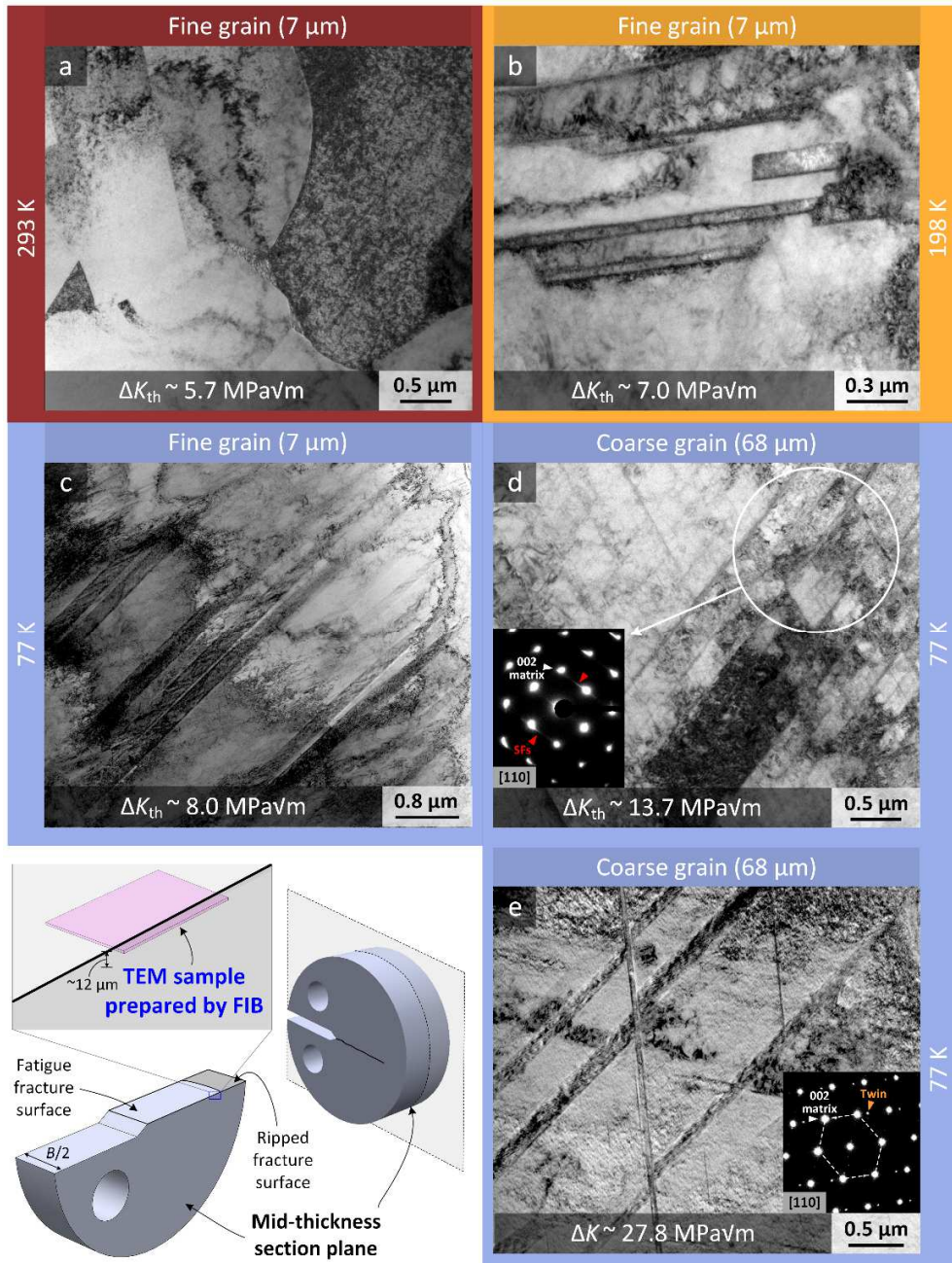


Fig. 10. TEM characterization of the nano-twins and dislocations in the plastic wake within 12 μm of the fatigue fracture surface. Deformation nano-twins are absent in the plastic wake in the fine-grained alloy in the near-threshold regime (a) at 293K and (b) 198K, but are evident (c) at 77K. (d) In the coarse-grained alloy tested in the near-threshold regime at 77K, nano-twins are not observed; however, profuse

stacking faults and planar slip bands can be readily seen. (e) Twin-twin network formed by deformation nano-twins with multiple variants can be seen in the coarse-grained alloy tested at a higher $\Delta K \sim 28$ MPa \sqrt{m} at 77K. Note that the twin lamella shown in (b) are annealing twins rather than deformation twins.

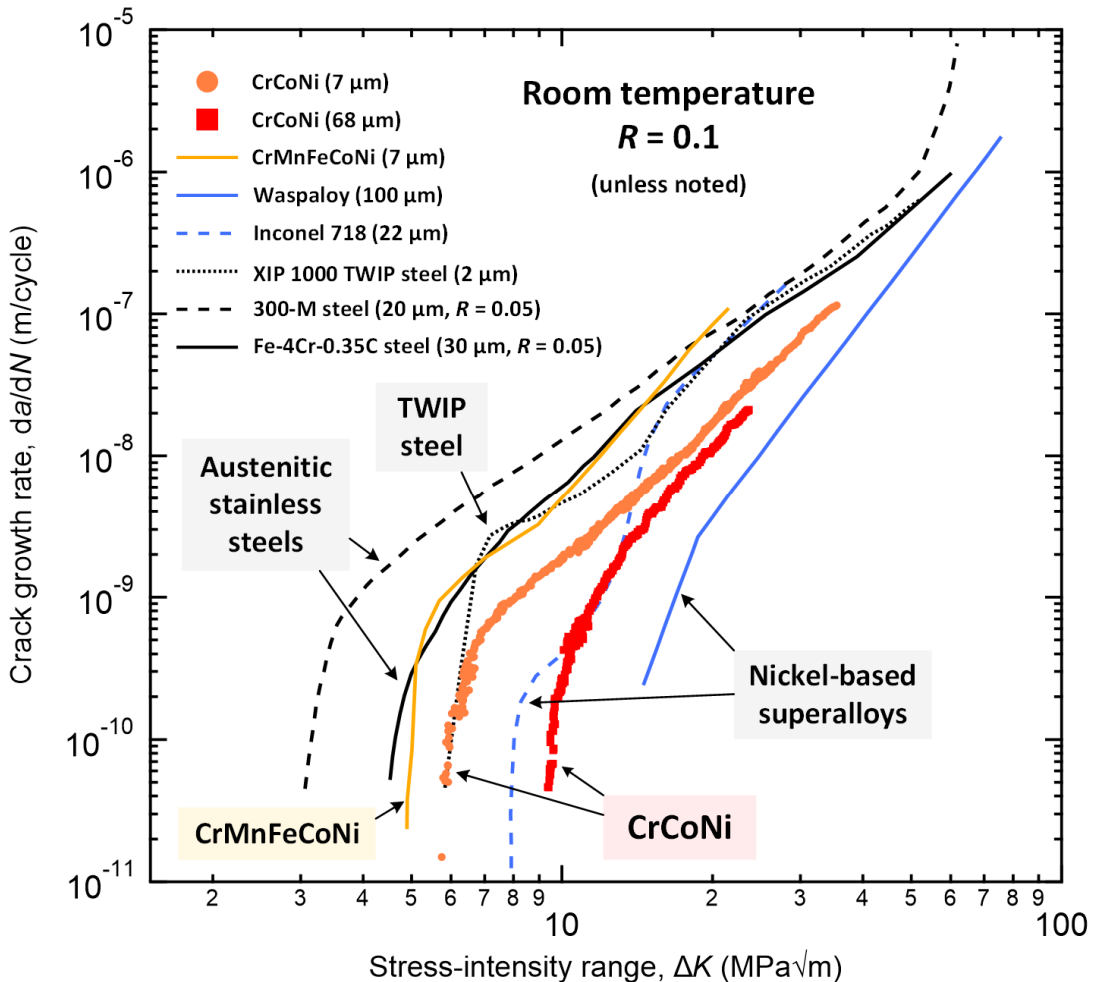


Fig. 11. Comparison of the crack-propagation fatigue behavior of the CrCoNi MEA with the CrMnFeCoNi high-entropy alloy and several other comparable structural alloys: specifically, austenitic stainless steels [46], twinning-induced plasticity (TWIP) steels [54], and nickel-based superalloys [55–57].

